

STABILITY ANALYSIS OF A SEGMENTED FREE-WING CONCEPT FOR UAS GUST
ALLEVIATION IN ADVERSE ENVIRONMENTS

Except where reference is made to the work of others, the work described in this thesis is my own or was done in collaboration with my advisory committee. This thesis does not include proprietary or classified information.

Jason Welstead

Certificate of Approval:

Brian S. Thurow
Assistant Professor
Aerospace Engineering

Gilbert L. Crouse Jr., Chair
Associate Professor
Aerospace Engineering

John E. Cochran Jr.
Professor and Head
Aerospace Engineering

George T. Flowers
Dean
Graduate School

STABILITY ANALYSIS OF A SEGMENTED FREE-WING CONCEPT FOR UAS GUST
ALLEVIATION IN ADVERSE ENVIRONMENTS

Jason Welstead

A Thesis

Submitted to

the Graduate Faculty of

Auburn University

in Partial Fulfillment of the

Requirements for the

Degree of

Master of Science

Auburn, Alabama
August 10, 2009

STABILITY ANALYSIS OF A SEGMENTED FREE-WING CONCEPT FOR UAS GUST
ALLEVIATION IN ADVERSE ENVIRONMENTS

Jason Welstead

Permission is granted to Auburn University to make copies of this thesis at its discretion, upon the request of individuals or institutions and at their expense. The author reserves all publication rights.

Signature of Author

Date of Graduation

VITA

Jason Robert Welstead, son of Robert "Bob" L. Welstead and Teresa "Tess" A. Welstead, was born on September 25, 1984 in Sioux City, Iowa. He attended school in Elkhorn, Nebraska where he participated in choir, soccer, and OPPD Powerdrive. In 2003, he graduated with honors from Elkhorn High School and the following fall enrolled to Wartburg College in Waverly, Iowa. Balancing collegiate athletics and academics, he graduated summa cum laude with a B.A. in Engineering Science and Mathematics in 2007. In the fall of 2007, he began his graduate studies at Auburn University. At Auburn University, he was the team leader of the American Institute of Aeronautics and Astronautics (AIAA) Design/Build/Fly student competition where the team successfully completed all three missions. Only 9 teams completed all missions out of a total of sixty. The following year, he was an advisor to the team that had a successful prototype four months before the competition. Directing numerous improvements, the team went to competition and successfully met the goal of having the lightest aircraft at the competition. In April of 2009, he presented and published a technical paper at the AIAA Unmanned...Unlimited conference which formed the foundation for this thesis.

THESIS ABSTRACT

STABILITY ANALYSIS OF A SEGMENTED FREE-WING CONCEPT FOR UAS GUST
ALLEVIATION IN ADVERSE ENVIRONMENTS

Jason Welstead

Master of Science, August 10, 2009
(B.A., Wartburg College, 2007)

112 Typed Pages

Directed by Gilbert L. Crouse Jr.

High altitude, long endurance (HALE) aircraft feature large wing spans and have very low wing loadings resulting in sensitivity to turbulence. While turbulence is usually quite low in the stratosphere where HALE aircraft typically operate, even high altitude aircraft must transition through the lower atmosphere during takeoff and landing operations. Sensitivity to turbulence may restrict the weather conditions under which HALE aircraft can be launched or retrieved. A compounding consideration for HALE aircraft is that because of their large wing spans, their wings may be longer than the length scale of the turbulence they encounter. This means that different portions of the aircraft's wings will see different aerodynamic conditions and will result in significant additional structural loads on the wing structure. Alleviating the aircraft's response to time-varying gust fields as well as spatially-varying gust fields is thus important for HALE aircraft. One promising technology for gust alleviation is the "free wing". A free-wing design allows the wing to adjust itself in pitch about a spanwise axis in response to aerodynamic loads rather than being rigidly attached

to the aircraft fuselage. Free wings historically have shown the ability to reduce an airplane's response to turbulence. An extension of the concept proposed here is called a "segmented free wing". A segmented free wing differs from the conventional free wing by sectioning the wings into multiple, independent segments. This design provides a greater reduction in turbulence response than both the standard free wing and the fixed wing as demonstrated in initial wind tunnel tests. A conceptual design of such a planform along with a study of its stability characteristics was examined. Initial results from a wind tunnel model showed a reduced rolling moment coefficient when compared to a traditional free-wing design. Experimental tests of the larger model showed a divergent oscillatory mode that appears with increasing velocity. An analytical model of the experimental test was developed and successfully predicts the instability. Comparison of the analytical model versus the experimental results shows an over-prediction of the stability of the system by the analytical model and causes for the over-estimation were investigated. The effects of unsteady aerodynamics, apparent mass terms, and wake effects on the analytical model were studied and all were determined to significant in the aerodynamic model. The analytical model was used to predict the crossover velocity of a wind tunnel model but the wind tunnel model failed to become unstable due to the stabilizing friction force in the bearing surfaces.

ACKNOWLEDGMENTS

The author would like to thank Dr. Gilbert L. Crouse Jr. for giving him the opportunity to work on this research. Dr. Crouse has been invaluable in his support on the research project. The author would also like to acknowledge Dr. Robert S. Gross for allowing him to use his vehicle to obtain experimental data. The author would like to thank Brian C. Reitz for his help with the electronics for the experimental model and working with the RC transmitter. Kevin Albarado's help with the wind tunnel testing was extremely appreciated. Finally, the author would like to thank Neal A. Allgood for his help in the construction of the experimental model.

Style manual or journal used American Institute of Aeronautics and Astronautics
(AIAA)

Computer software used Matlab 7, Microsoft Word 2007, Microsoft Excel 2007,
WinEdt, Latex, Microsoft Paint, QuickTime, Adobe Photoshop

TABLE OF CONTENTS

LIST OF FIGURES		xi
LIST OF TABLES		xiv
1 INTRODUCTION		1
2 REVIEW OF LITERATURE		5
2.1 Active Control Systems		6
2.2 Passive Control Systems		9
3 CONCEPTUAL DESIGN		13
3.1 Sizing and Configuration		13
3.2 Airfoil Design		14
3.3 Experimental Setup		16
3.4 Wind Tunnel Model		17
4 ANALYTICAL MODEL		21
4.1 Governing Equations		22
4.2 Aerodynamics		23
4.2.1 Validation of Aerodynamic Model		29
4.3 Wake Effects		33
4.4 Equations of Motion		37
4.5 Wind Tunnel Model		39
5 RESULTS		40
5.1 Initial Wind Tunnel Test		40
5.2 Experimental Model		41
5.3 Analytical Modeling		46
5.3.1 System Properties		47
5.3.2 Analytical Model Without Fixed Segments		52
5.3.3 Analytical Model With Fixed Segments		57
5.3.4 Analytical Model Compared to Experimental Results		62
5.3.5 Full Aerodynamic Model Sensitivities		64
5.3.6 Variation of Input Parameters Based Upon Error Estimates		70
5.3.7 Modeling Options		74

5.4	Wind Tunnel Model	82
5.4.1	Wind Tunnel Test Results	82
5.4.2	System Properties	84
5.4.3	Analysis of Results	84
5.4.4	Friction Discussion	88
6	CONCLUSIONS	92
7	FUTURE WORK	95
	BIBLIOGRAPHY	96

LIST OF FIGURES

1.1	Cross-sectional illustration of the free-wing design	2
3.1	Segmented free wing viewed from the top	13
3.2	Free-wing airfoil design with control tab	14
3.3	Lift coefficient versus angle of attack	15
3.4	Pitching moment versus lift coefficient	16
3.5	Diagram of the experimental setup	17
3.6	Segmented free wing mounted to beam on truck looking through the windshield	18
3.7	Wind tunnel test schematic	19
3.8	Segmented free-wing model in AU wind tunnel	20
4.1	Axis configuration for analytical model	21
4.2	Free-body diagram of the segmented free-wing system in roll, looking from rear	22
4.3	Free-body diagram of a wing segment	23
4.4	The real and imaginary parts of Theodorsen's function, $F(k)$ and $G(k)$ respectively	25
4.5	Comparison of the analytical model circulatory lift to Theodorsen's function	31
4.6	Comparison of the analytical model total lift response with pitching data from Rainey	32
4.7	Setup of the Vortex Lattice Method on segmented free wing	33

4.8	“Nomenclature for calculating the velocity induced by a finite length vortex segment”	35
5.1	Segmented free wing with fixed segments attached to the tip flying with a visible dihedral	45
5.2	Diagram of the bifilar pendulum setup	47
5.3	Experimental model mounted on the bifilar pendulum in Auburn University’s Adaptive Aerostructures Lab	50
5.4	Experimental segment mounted on the bifilar pendulum in Auburn University’s Adaptive Aerostructures Lab	51
5.5	Axis orientation for modulus calculations	52
5.6	Root locus plot of the full aerodynamic model for the mechanically restrained model without fixed segments	53
5.7	Root locus plot of the full aerodynamic model for the mechanically restrained model without fixed segments from a zoomed in perspective	54
5.8	Root locus plot for the full aerodynamic model for the system mechanically free in roll without fixed segments	55
5.9	Root locus plot for the full aerodynamic model for the system mechanically free in roll without fixed segments zoomed in about the origin	56
5.10	Root locus plot for the full aerodynamic model for the system mechanically restrained in roll with fixed segments	58
5.11	Root locus plot for the full aerodynamic model for the system mechanically restrained in roll with fixed segments attached, zoomed about the origin	59
5.12	Root locus plot for the full aerodynamic model for the system mechanically free in roll with fixed segments attached	60
5.13	Root locus plot for the full aerodynamic model for the system mechanically free in roll with fixed segments attached, zoomed in about the origin	61
5.14	Full aerodynamic model sensitivity to changes in pitching mass moment of inertia	65

5.15	Full aerodynamic model sensitivity to changes in rolling mass moment of inertia	66
5.16	Full aerodynamic model sensitivity to changes in the aerodynamic center	67
5.17	Full aerodynamic model sensitivity to changes in the center of gravity position	68
5.18	Full aerodynamic model sensitivity to changes in the spring constant K	69
5.19	Root locus plot of the full aerodynamic model with modified input parameters but without fixed segments	72
5.20	Root locus plot of the full aerodynamic model with modified input parameters but without fixed segments zoomed in to reveal unstable roots	73
5.21	Root locus plot of the basic model	75
5.22	Root locus plot of the basic model with wake effects	77
5.23	Root locus plot of the basic model with unsteady aerodynamics . . .	79
5.24	Root locus plot of the basic model with apparent mass terms	80
5.25	Root locus plot of the full aerodynamic model	81
5.26	Root locus plot for the wind tunnel model	85
5.27	Friction coefficients for maintained stability with unsteady aerodynamics	86
5.28	Friction coefficients for maintained stability without unsteady aerodynamics	87

LIST OF TABLES

5.1	Rolling moments of three configurations	41
5.2	Results of the experimental testing on the segmented free wing	43
5.3	Lodgepole Pine elastic properties	50
5.4	Data from spring constant test on mounting beam	52
5.5	Results of the different modeling features	76
5.6	Selected values of coefficients of friction	89

CHAPTER 1

INTRODUCTION

Turbulence in the troposphere has long been an issue for aircraft of all sizes. However, aircraft with lower wing loadings are much more sensitive to turbulence than aircraft with high wing loadings. The high sensitivity to turbulence as seen in general aviation aircraft and unmanned aerial systems (UAS) causes passenger discomfort, sensor malfunction, or potentially fatal loss of control. High altitude, long endurance (HALE) aircraft are even more sensitive to turbulence than the standard UAS or small aircraft because of their very low wing loading and light construction. An example of this type of problem is demonstrated in NASA's Helios project, a HALE aircraft with a wing span of 247 feet. The Helios aircraft took off from Kauai, Hawaii on June 26, 2003 and flew approximately 30 minutes until a divergent pitch oscillation occurred "in which the airspeed excursions from the nominal flight speed about doubled every cycle of the oscillation." The design speed of the aircraft was subsequently exceeded causing dynamic pressures to increase beyond the designed limits of the structure. Under the intense load, the vehicle began to break up and it eventually crashed into the ocean. The final determination of the crash investigation was that the fatal pitch oscillation was caused by atmosphere disturbances, i.e. turbulence, which resulted in a structural failure of the system [1].

A possible solution to this sensitivity to turbulence is to increase the wing loading to be comparable to that of airliners; however, this is unpractical in small aircraft [2] and UAS's, especially HALE aircraft. Reducing wing area of a HALE aircraft would

reduce wingspan and thus increase induced drag thereby greatly reducing its maximum altitude and endurance capabilities. Reducing wing area would also increase stall speed which would negatively affect safety of operation. Another solution is to increase the structural strength of the HALE aircraft to handle the dynamic loading under oscillatory conditions. However, this would increase the system weight which would decrease performance taking away from the HALE mission.

Alternatively, an approach to decrease the sensitivity to turbulence is a free-wing design as depicted in Fig. 1.1. A free wing differs from a fixed wing in that the wing is

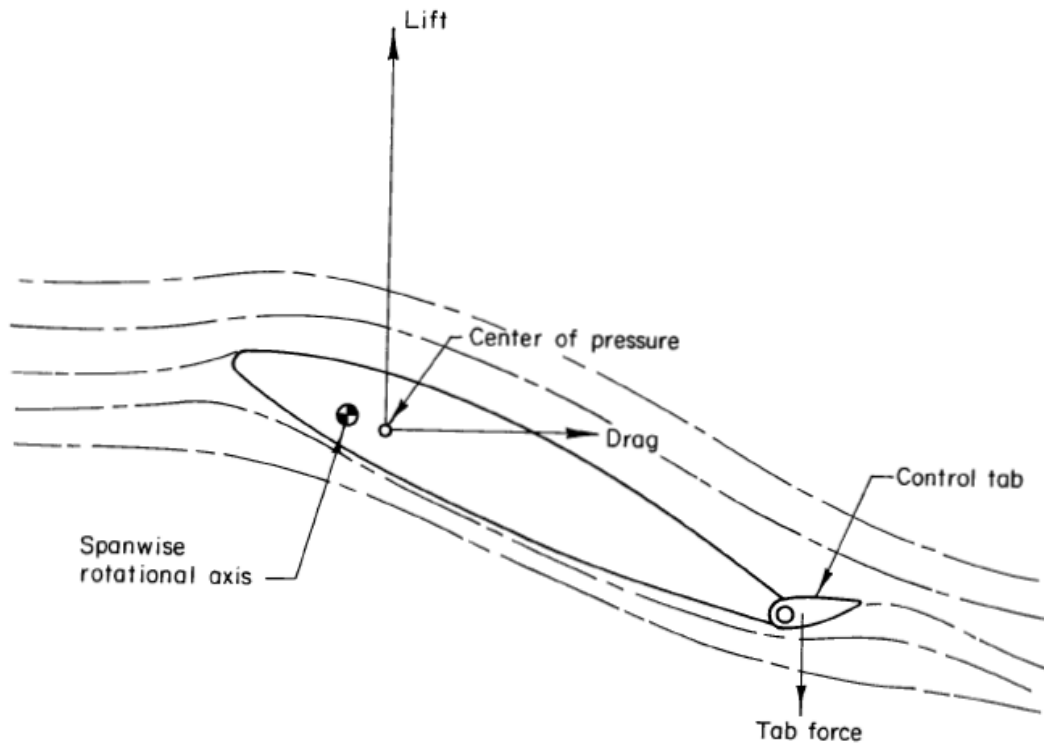


Figure 1.1: Cross-sectional illustration of the free-wing design [3]

free to pivot about a spanwise axis. Another difference is that the aerodynamic forces control the pitch of the wing, whereas, with a fixed wing the fuselage controls the pitch of the wing. A control tab on the trailing-edge of the wing is the only control device

used to increase or decrease lift. NASA conducted several studies on the free-wing planform throughout the 1970's and early 1980's dealing with aircraft ranging from 3,000 to 50,000 pounds [3]. It was determined in Ref. [3] that the free wing drastically reduced the load-factor response, as high as 4 to 1 in all configurations. The major conclusion from the study was that the free wing was extremely effective at reducing the longitudinal response to disturbances for aircraft of common wingspans.

A limitation of the free-wing planform is that it can only adjust to time-varying turbulence. A feature of HALE aircraft is their large wingspans which makes them susceptible to both time-varying and span-varying turbulence. The extension to the free-wing concept proposed here is called a segmented free wing and breaks the wing into multiple independent free-wing segments. Each segment is allowed to move and to be controlled independently from all of the other segments. The segmented free-wing design shows promise for application to HALE aircraft due to its ability to adjust to both time-varying and span-varying turbulence. Being a passive system, just like the free wing, no complex control systems need to be designed and implemented into the system; thus saving system complexity and weight. Each segment is free to pivot about its span-wise axis allowing the entire wing to maintain a constant angle of attack even as the velocity field is changing. Additionally, the wing can alter its local pitch as disturbances vary across the span of the wing. Regardless of the turbulence profile across the planform, the segmented free wing can adjust to maintain constant lift across the span and alleviate much of the lateral response of the aircraft. With this ability to deal with both time-varying and span-varying turbulence, the segmented free wing is ideal for use in HALE aircraft design.

The initial thrust of this research was to design and fabricate a conceptual model and perform preliminary testing on the model. With the preliminary testing, the study of the dynamic stability of the segmented free wing became the focus of this

research. An experimental model was constructed and tested to determine the stability of the system. An analytical model was also developed to model the behavior of the segmented free wing and to predict the stability of the system. A wind tunnel model was constructed to give preliminary results of the spanwise varying turbulence response, along with testing the validity of the analytical model.

CHAPTER 2

REVIEW OF LITERATURE

Aircraft gust response is a topic that has been studied extensively since the early 1900's when the Wright Brothers were ushering in the new age of flight. It is an area of intense interest due to its affect on passengers and the increased requirements it places on the strength of the aircraft structure. Additionally, the aeroelastic effects of the aircraft's gust response can potentially lead to negative damping of a structural or flight mechanics mode causing extremely large, potentially fatal vibrations or oscillations. Not only can the gust response of an aircraft cause structural problems, it also creates issues with passenger comfort and scientific equipment. Air travelers often avoid smaller aircraft due to their magnified gust response when compared to heavier aircraft. Additionally, aircraft flying scientific missions in extremely adverse environments, such as hurricanes, may require sensitive instruments that could be damaged or their effectiveness degraded by the gust response of the aircraft. Aircraft flying High Altitude, Long Endurance (HALE) missions typically have extremely high aspect ratios with low wing loadings and thus are more sensitive to adverse gust loadings. The low fuel fractions and light structure of HALE aircraft result in an aircraft that is both flexible and sensitive to adverse gust conditions. Flight dynamics of very flexible aircraft were studied by Shearer and Cesnik [4] where they implemented 6-DOF vehicle dynamics with a modified version of the non-linear strain-based structural formulation originally developed by Cesnik and Brown [5]. In their heavy weight cases, rigid-body solutions were not sufficient to accurately capture the flight dynamics of

flexible aircraft. Shearer and Cesnik also determined that linear analysis was sufficient for modeling simple symmetric maneuvers but nonlinear analysis was required to accurately model the vehicle response due to asymmetric maneuvering. An understanding of the nonlinear flight dynamics of flexible aircraft is necessary as shown by Cesnik and Brown, but solutions for dealing with the adverse gust conditions causing the nonlinear flight dynamics are needed.

Two broad categories of methods for alleviating the gust response have been researched. One is active control systems where the aircraft actively responds based on measurements of its flight conditions. This has been a topic of more recent research with the advancement of new materials and computing capabilities for active control laws. The second is passive systems whereby the aircraft automatically responds to the flight conditions without any active control inputs or measurements. This is extremely beneficial in that it maintains simplicity of the design. The second method is the focus of this research.

2.1 Active Control Systems

Active control systems and aeroservoelasticity have been a popular area of research in addressing gust alleviation. A difficult problem with using active control systems has been accurately modeling the aerodynamic behavior of the system so control laws could be derived. The Laplace domain has been used to calculate the unsteady aerodynamic loads and aerodynamic coefficients which tend to be nonrational and mathematically intensive [6], [7]. A finite-order, state-form, matrix equation for stability analysis is desired which requires the aerodynamic influence coefficients to be approximated [6]. Because of the complexity of these calculations and the nonrationality of the coefficients, a rational approximation of the unsteady loads on a

typical section in incompressible flow was formulated by R. T. Jones [8]. Approximating the nonrational coefficients caused a degradation in the accuracy of the model but is necessary to be implemented into the control systems [9]. Karpel [6] developed a new minimum-state method for efficiently approximating rational unsteady aerodynamic loads. With an acceptable approximation of the unsteady aerodynamic loads, a state-space set of matrix equations could be formulated and control laws implemented for the active control system [6].

Within active control systems, two methods that were studied provide increased system performance by reducing the gust response and delaying/eliminating the onset of flutter. The first method used aerodynamic control surfaces such as ailerons and the second used aeroservoelasticity to alleviate the gust response. Block and Gilliat [10] successfully doubled the stability of a simple wing with the use of a single control surface that was 20% of the wing and spanned the entire trailing edge. Cruise flaps, similar to the previous study, were shown to successfully reduce disturbances in aircraft lift and vertical acceleration at the aircraft center of gravity by 65%. Measurements of the pressure differentials allowed the cruise flap to adjust and maintain the ideal stagnation point in adverse gust conditions [11]. Additionally, Rennie and Jumper [7] used a trailing-edge flap on a NACA 0009 airfoil that was 27% of the chord. Measurements of the lift perturbations and the pressure distributions were used to control the flap and successfully reduce the gust response. Several problems exist with these methods of gust alleviation. First, the control surface must be significant in size as characterized by all three studies where the control surface was at least 20% of the chord. Additionally, as determined by the trailing-edge flap study [7], the control rates for the flap were high and the lift and pressure measurements to determine the aeroelastic properties were extensive adding system complexity. Also,

Ref. [11] was limited in its results because it did not include the aeroelastic effects of the unsteady aerodynamics resulting from the rapid flap motion.

Research has been conducted to see if an optimization algorithm can be used to optimize the planform design in order to have the greatest aeroelastic control for a given design using control surfaces [12], [13]. Nam and Chattopadhyay [13] varied aspect ratio, sweep angle, control surface location, and control surface size whereas Pettit and Grandhi [12] used aileron effectiveness and gust response as the driver of the design. In both cases, the gust response of the designed aircraft was reduced when compared to a base model.

An approach different to using standard control surfaces for gust alleviation is to use several special control surfaces. Instead of a single trailing-edge control surface, Moulin and Karpel [9] used three control surfaces: ailerons, special underwing forward positioned control surfaces, and special wing-tip forward-positioned control surfaces. At intermediate velocities, the movement of all control surfaces successfully reduced the gust loads and the wing tip accelerations in the wind tunnel tests. However, as the velocity was increased the effectiveness of the ailerons was reduced but the special surfaces became more efficient with the wing-tip surfaces being the most efficient.

Another active control system involved manipulating the aeroelastic properties of the system in order to produce beneficial results, otherwise known as aeroservoelasticity. The use of piezoelectric materials was studied on a cantilevered composite plate to determine if aeroservoelastic control was capable of reducing the gust response. Using four actuator units, “tip displacement, twist, and acceleration [were] reduced by 36%, 72%, and 54% respectively” [14]. Additionally, Lazarus, Crawley, and Lin [15] used actuators to control both the shape and the strain forces of the lifting surface. By controlling those two parameters, the dynamic stability of the lifting plate was increased. Use of the strain-actuated lifting surface reduced the rms gust

response by 60% in addition to the flutter speed being increased by 11%. Several problems with aeroelasticity consist of the power required by the actuators to deform the surface appropriately. This especially becomes a problem as the thickness ratio of the lifting surface is increased beyond that of a thin plate [15]. Along with the power requirement, the actuator size increases as the thickness ratio becomes larger. Finally, the density of the piezoceramics used in aeroservoelastic control is more than double that of aluminum, which makes it an extremely unfriendly aircraft material.

Overall, active control systems show promise in being able to successfully alleviate or reduce the gust response of an aircraft if properly designed. The drawbacks of using active control systems for gust alleviation are the increase in system complexity, computing power, weight, sizing, and maintenance. In order to properly model the aeroelastic properties of the wing, additional sensors need added and implemented into the controller which is nontrivial. The additional weight of the sensors, wires, actuators, and control surfaces can also add up quickly. Finally, a significant financial cost will be associated with the maintenance of these systems.

2.2 Passive Control Systems

A passive control system for gust alleviation in aircraft is the torsionally free wing, otherwise known as the “free wing”. The free-wing design allows the wing to freely rotate about a spanwise axis, usually the structural spar, where the aerodynamic forces control the pitch of the wing. Extensive research was conducted on the free wing by NASA throughout the late sixties through the early 1980’s. The first major study of the free wing was conducted by Porter and Brown in 1970 where the stability and gust alleviation properties were studied analytically [3]. Three separate aircraft classes were considered to analyze the capabilities of the free wing. A general aviation

(Cessna style) aircraft, a utility aircraft, and a transport aircraft were all analyzed using the free wing. In all flight regimes, the gust responses of all three aircraft classes were significantly decreased. Along with the excellent reductions in gust response, results showed a 25% reduction in roll disturbances as well [3].

Additional studies on the aerodynamics and the potential for dynamic stall and flutter of the free wing were studied by Ormiston in 1972 [16]. Dynamic stall and flutter characteristics were achievable with the free wing but could be easily eliminated by the reduction in the size of the trailing-edge control tab. With a properly designed control tab, the stability characteristics of a free-wing wing section were excellent and maintained the extreme difficulty in stalling the wing.

As a followup to Porter and Brown [3], results of a study of the applications of the free wing for light, general aviation aircraft were reported in Ref. [17]. It was determined that the free wing could be applied to light, general aviation aircraft because of the excellent gust alleviation characteristics of the free wing. A 54% reduction in the rms load factor was found when the aircraft was subjected to continuous turbulence. A “free-wing/free-trimmer” design was studied by NASA in 1978 where the free-trimmer was a free-wing design that controlled the pitch angle of the main free wing [18]. The same beneficial gust alleviation was experienced but the free-trimmer increased the maximum lift capability when compared to a pure free-wing configuration.

The free-wing design was most effective in aircraft that have low wing loadings, such as light, general aviation aircraft and many unmanned aerial vehicles. The greater the wing loading, the less the turbulence response. However, having a low wing loading free-wing aircraft was like having a fixed wing aircraft with a large wing loading. This was shown in Ref. [2] where the free-wing design had a similar peak vertical acceleration from the vertical gust profile as a high wing loading fixed wing.

A fixed wing aircraft with a wing loading similar to that of the free-wing aircraft had a vertical response five times greater.

Free wings have been considered for the use in unmanned aerial vehicles. Unmanned aerial vehicles have become increasingly popular for use in long endurance missions, experimentation, and surveillance. Kraeger [19] studied the use of a free-wing UAV for a microgravity facility where the UAV could fly exact mission profiles at a lower cost compared to larger microgravity facilities operated by manned aircraft. A fixed wing UAV microgravity facility was more sensitive to gusts compared to the much larger manned microgravity facility. The gust response could cause the UAV to deviate from the ideal flight path and be detrimental to the microgravity performance. The free-wing UAV microgravity facility was capable of handling these disturbances and maintain the desired microgravity flight performance.

The free wing is a passive control system that is very capable of alleviating gust and rolling disturbances on aircraft of all sizes. A great benefit of the free wing is that it requires no wiring, no computer power, no power to work any actuators other than the trailing edge control tab which is no different than an aileron, and maintains simplicity so maintenance and maintenance costs would be considerably less than an active control system. A drawback of the free wing is the loss of maximum lift when compared to a fixed wing aircraft. Because the trailing edge of the free wing is used to control the pitch of the wing, the maximum lift produced by the wing was significantly reduced and leading edge flaps were highly suggested to make up for the lost lift [17]. Additionally, a weight penalty is usually incurred using the free wing due to the ballast required to balance the free wing on the spanwise hinge axis. The loss can be as much as 1.5% to 7% of the aircraft gross weight depending on the location of the hinge axis [17]. Finally, when the right and left wings are free to rotate

with respect to each other, an unstable spiral mode exists that must be stabilized, especially in the lower flight speeds [3].

CHAPTER 3
CONCEPTUAL DESIGN

3.1 Sizing and Configuration

A conceptual design was created in order to study the stability characteristics of the segmented free-wing system and to test its gust response for use on a HALE aircraft. The segmented free wing was designed to fit onto an existing, modular testbed aircraft by replacing the existing fixed wings of the aircraft. The overall wingspan of the system was approximately 13.3 feet and had a chord of 16 inches. The planform had no taper or sweep. Each half of the wing was divided into 5 equal segments approximately 14 inches wide with a 1/16 inch gap between each segment to prevent any interference between segments. A top view of the segmented free wing is shown in Fig. 3.1. Each individual segment was balanced about its hinge

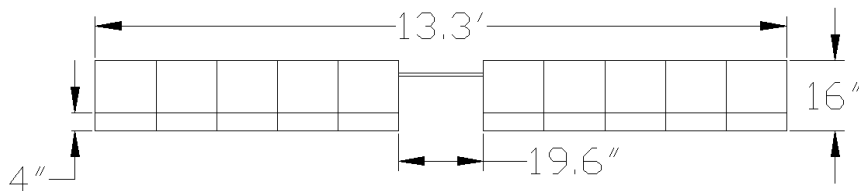


Figure 3.1: Segmented free wing viewed from the top

axis by adding counterweights extending in front of the segment. The total weight of the wing was 8.5 pounds including the counterweights.

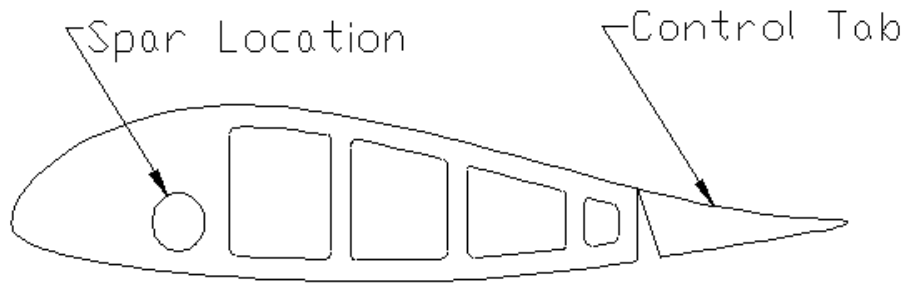


Figure 3.2: Free-wing airfoil design with control tab

3.2 Airfoil Design

To maintain static pitch stability of each wing segment the pivot axis must be ahead of the aerodynamic center of the segment, which is most often near the quarter-chord [3]. The hinge margin is the distance the pivot axis is ahead of the quarter-chord line and is represented in percentage of the chord. Hinge margins ranging from $0.05c$ to $0.20c$ were examined in Ref. [3]. Additionally, the effect of the hinge margin on the control tab sizing at the trailing edge of the wing was examined [3]. In this study, a hinge margin of $0.05c$ was chosen in order to reduce the amount of ballast required to balance the wing segments. With this hinge margin the pivot axis, which was the main wing spar, was located at 20% of the chord. Vertically, the spar was centered on the chord line.

A control tab was located at the trailing edge and was the only control device on the segmented free wing. The control tab could deflect ± 20 degrees, had a chord length of 25% of the wing chord, and spanned the entire trailing edge of the segment. Each segment's control tab was actuated using an electric servo motor embedded in the airfoil and covered using a plastic skinning material.

The airfoil shape selected was an airfoil designed by John Roncz for Freewing Aerial Robotics and used on their Scorpion UAV. This airfoil shape is shown in Figure 3.2. The wing was constructed out of extruded polystyrene foam. Several sections of the inner wing were cut out to allow the passing of wires and to reduce weight. A counterweight was attached to the bottom side of each segment and extended forward of the leading edge with approximately a 1 oz weight attached. The counterweight moved the center of gravity forward to balance the segment on the spanwise pivot axis.

The airfoil was analyzed using Xfoil [20], [21] to determine its aerodynamic center and lift curve slope. A Reynolds number was calculated to be around 200,000 based upon a 22 *ft/s* velocity and a 16 inch chord length. This was used for the viscous boundary layer analysis. As shown in Fig. 3.3, the lift curve slope, C_{l_α} , was calculated to be 7.66 per radian (0.132 per degree). Figure 3.4 shows the pitching moment of

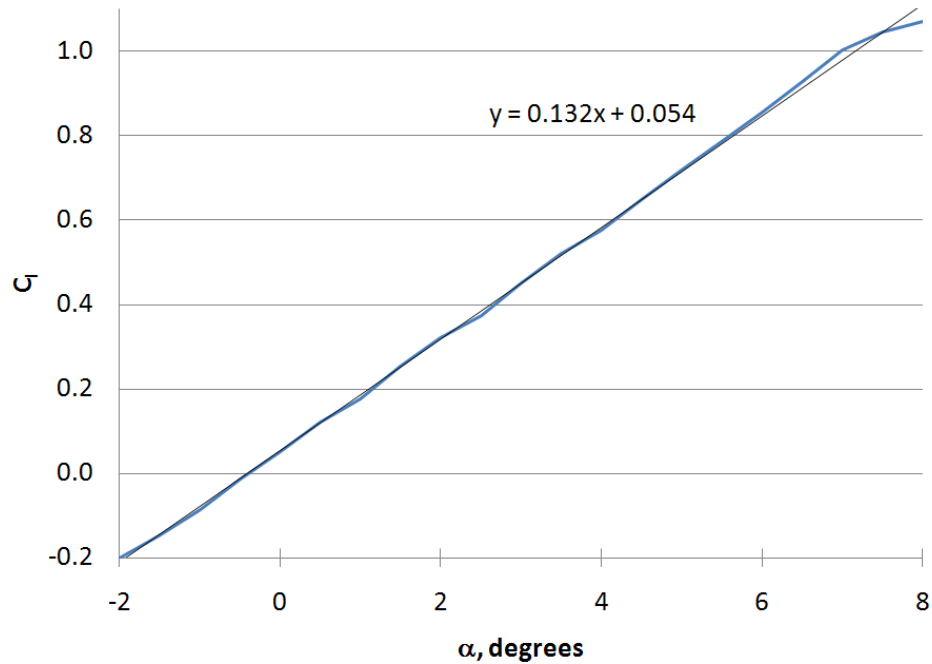


Figure 3.3: Lift coefficient versus angle of attack

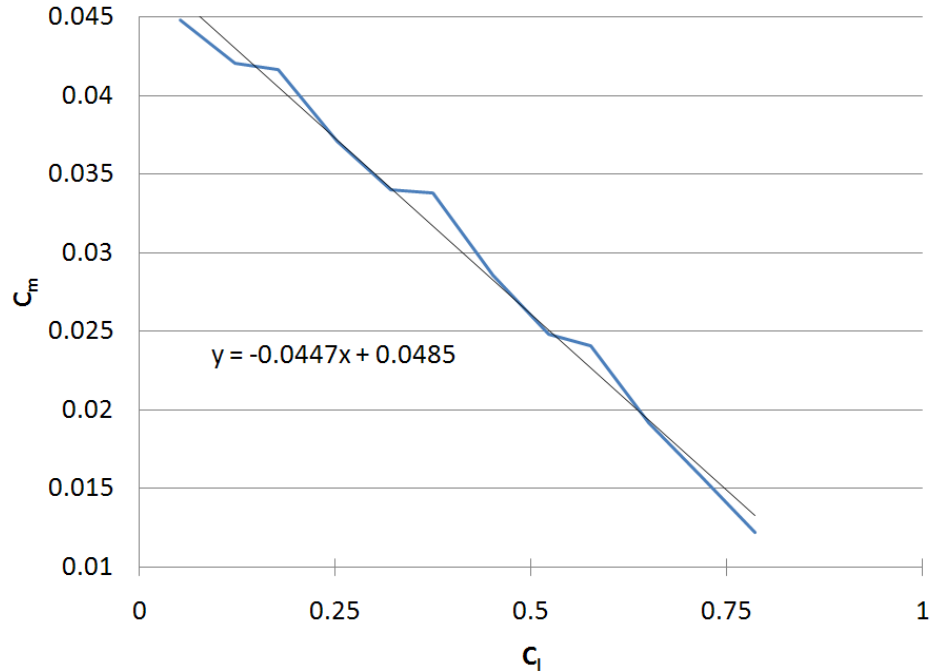


Figure 3.4: Pitching moment versus lift coefficient

the airfoil about its 1/4 chord point as a function of lift coefficient. A linear trend line from regression analysis has been drawn on the graph along with the trend line equation. The aerodynamic center of the airfoil was found by adding 1/4 to the inverse slope of the trend line. At 29% of the chord, the aerodynamic center for this airfoil is considerably further aft than the typical thin airfoil value of 25% of the chord.

3.3 Experimental Setup

The segmented free-wing model was tested experimentally by mounting the model on a truck. The wing was mounted to a 3" x 3 1/2" wood beam (constructed from a pair of 2x4's) that extended 7 feet in front of the truck as shown in Fig. 3.5.

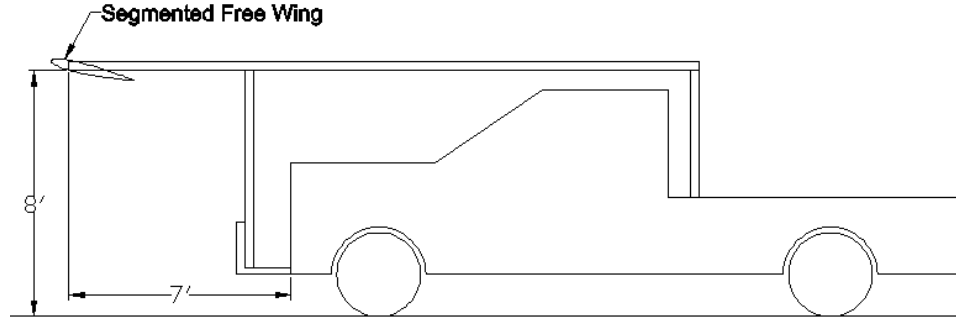


Figure 3.5: Diagram of the experimental setup

Mounting the wing a considerable distance in front of the truck reduced the aerodynamic influence of the truck on the wing. The wing was rigidly mounted to the beam so that roll was mechanically restrained. The mount was later modified to allow the wing to freely roll. The control tabs on each of the wing segments were controlled via a radio transmitter so the angle of attack of the segments could be varied from within the truck cab during testing.

3.4 Wind Tunnel Model

A wind tunnel model of the wing was designed and fabricated for use in the Auburn University 3x4 foot subsonic wind tunnel. The model had a wing span of three feet divided into six segments of equal size (approximately 6 inch span). Each segment had an eight inch chord with the axis of rotation placed at fifteen percent of the chord. Each segment had a negative five degree control surface deflection. Unlike the larger model discussed in Section 3.1, the wind tunnel model had no internal control wires. The wing segments were balanced about the pivot axis using lead shot so the only net forces acting on the wing segments were the aerodynamic forces. The spar was made of $\frac{1}{2}$ inch diameter steel round stock to maintain the stiffness in the model. A $\frac{1}{16}$ inch spacer was placed between each segment to prevent the



Figure 3.6: Segmented free wing mounted to beam on truck looking through the windshield

segments from interfering with each other. To create a spanwise flow variation in the wind tunnel, an oscillating wing was placed vertically in the wind tunnel generating a trailed vortex across the segmented free-wing wind tunnel model. A schematic of the wind tunnel setup can be seen in Fig. 3.7.

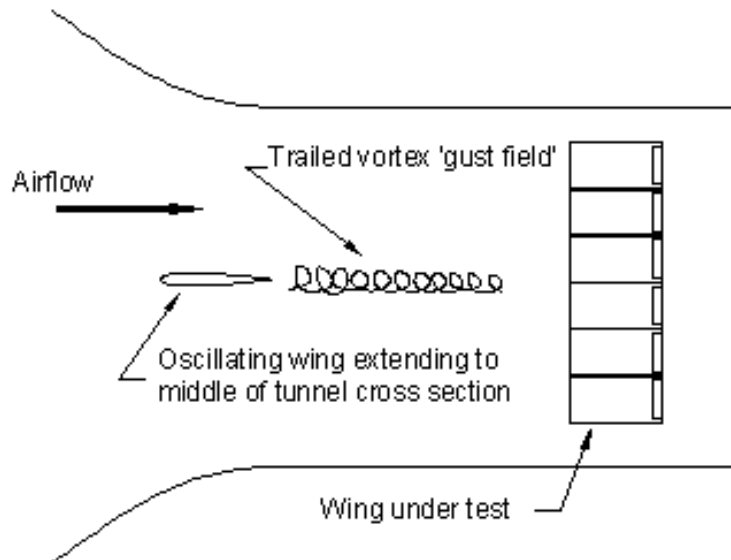


Figure 3.7: Wind tunnel test schematic

The wind tunnel model was designed so that each individual segment could be connected to its neighbors. Thus, it could simulate a single free wing, a left and right free wing, or a segmented free wing.

The variation in angle of incidence across the six segments is easily seen in Fig. 3.8 as each individual segment adjusts to maintain constant aerodynamic angle of attack across the span in the presence of the trailed vortex above the wing.

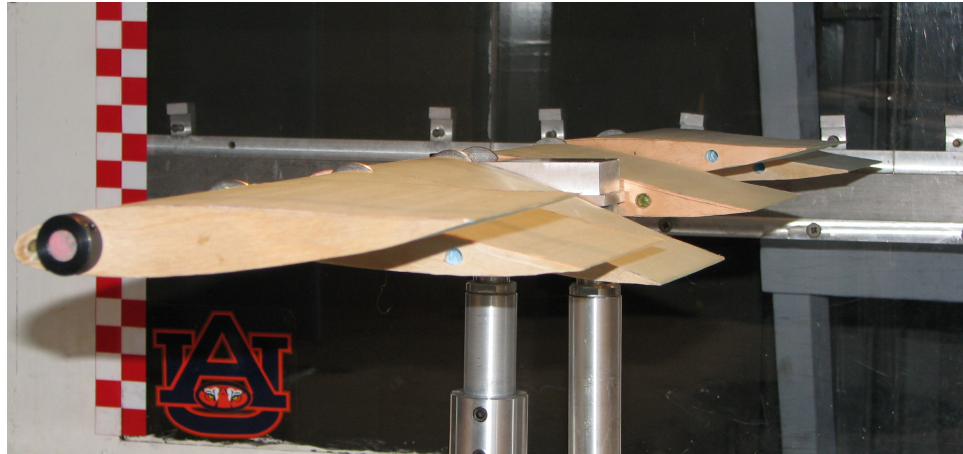


Figure 3.8: Segmented free-wing model in AU wind tunnel

CHAPTER 4
ANALYTICAL MODEL

A mathematical model of the segmented free wing was developed in order to accurately predict the behavior of the system. MATLAB 7.0 was used to run the calculations and to plot the results of the stability analysis. A linear model of the system dynamics was developed and eigen analysis was used to evaluate the behavior of the segmented free-wing system.

The origin of the system was located at the intersection of the axis of symmetry and the centerline of the spar. The x-direction points forward from the leading edge of the wings and y-direction extends out the right wing as shown in Fig. 4.1. The z-direction points downward to complete the triad. The system was modeled with 11 degrees of freedom: ten different pitch angles, one for each segment, and a roll angle. The system was mechanically restrained to the support beam resulting in no translational degrees of freedom. The translation of the truck was assumed to be a constant velocity in the x-direction.

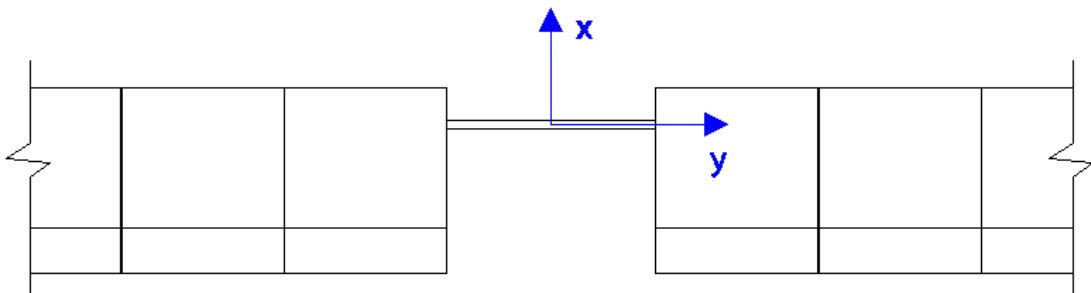


Figure 4.1: Axis configuration for analytical model

4.1 Governing Equations

Free-body diagrams of the segmented free-wing system and a wing segment are shown in Figs. 4.2 and 4.3. From the free-body diagrams, equations modeling the segmented free-wing system could be formulated.

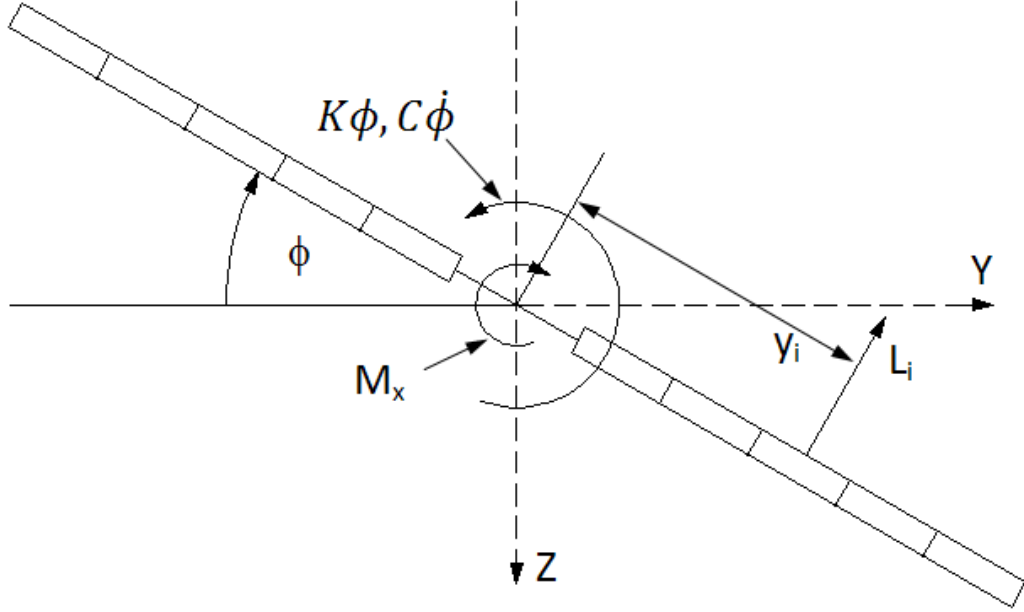


Figure 4.2: Free-body diagram of the segmented free-wing system in roll, looking from rear

The equation modeling rolling motion of the system is

$$\begin{aligned}
 M_x &= I_{xx}\ddot{\phi} \\
 M_x &= -\sum_i L_i y_i - K\phi - C\dot{\phi} + \sum_i m y_i \delta_{x_i} \ddot{\theta}_i
 \end{aligned}
 \tag{4.1}$$

where $\ddot{\phi}$ is the rolling acceleration in rad/s^2 , K is the spring force of the mounting beam, and C is the damping term in the wood. The final term in Eqn. 4.1 takes into

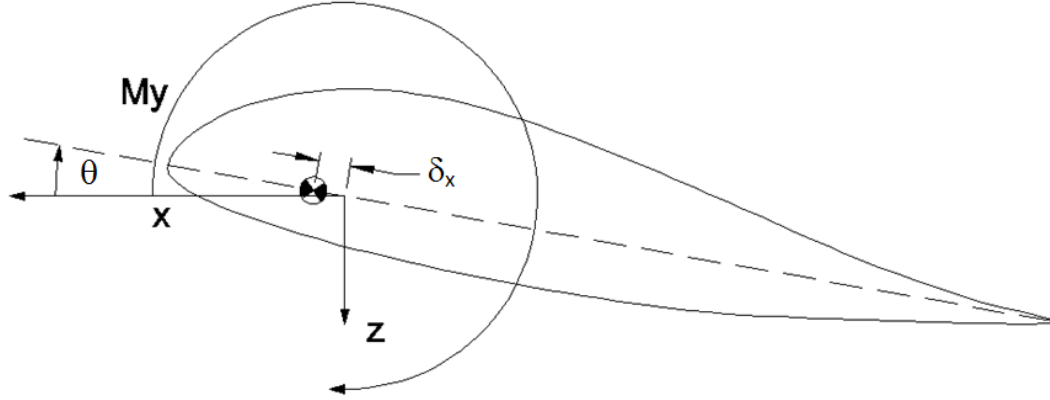


Figure 4.3: Free-body diagram of a wing segment

account the possible offset of the center of gravity of the wing segments causing a slight imbalance in each segment.

The equation for the pitching motion of each segment is

$$\begin{aligned}
 M_{y_i} &= I_{yy} \ddot{\theta}_i \\
 M_{y_i} &= M_{AERO_i} + m y_i \delta_{x_i} \ddot{\phi}
 \end{aligned}
 \tag{4.2}$$

where $\ddot{\theta}$ is the pitching acceleration in rad/s^2 , M_{AERO} is the aerodynamic moment, and the final term is the center of gravity offset.

4.2 Aerodynamics

The aerodynamic lift and moment, L_i and M_{AERO_i} , in Eqns. 4.1 and 4.2 are the most complex terms in the analytical model. Unsteady aerodynamic calculations were used to accurately model the aerodynamic forces and moments on the segmented free wing. To determine whether unsteady aerodynamics are significant for this problem or whether a quasi-steady approximation could be justified, a brief analysis using Theodorsen's function was completed. Theodorsen's function is one

method for modeling unsteady aerodynamics in the frequency domain. Theodorsen's function predicts the lift response, both in-phase and out-of-phase, to a sinusoidal oscillation of an airfoil as a function of the reduced frequency. Figure 4.4 presents the real (in-phase) and imaginary (out-of-phase) parts of Theodorsen's function for a range of reduced frequency. The reduced frequency can be calculated by

$$k = \frac{\omega b}{U} \quad (4.3)$$

where ω is the oscillation frequency in *rad/s*, b is half the chord length, and U is the velocity in feet per second [22]. During experimental testing of the model described in Section 3.1, an oscillation at a frequency of 1.2 Hz was observed at an airspeed of 22 fps. This corresponds to a reduced frequency of $k = 0.23$. Using Fig. 4.4, the magnitude of the lift response was 0.72 and the phase shift is 0.2584 rad or 14.80 degrees. This indicates that a quasi-steady assumption would over predict the lift response by over 20% and clearly unsteady effects are significant.

In unsteady aerodynamics the lift response to a step change in angle of attack, known as the indicial response, can be modeled as [23]

$$\frac{C_L(s)}{\Delta\alpha} = C_{L_\alpha}\phi(s) \quad (4.4)$$

where s represents the distance traveled in half chords

$$s = \frac{Ut}{b} \quad (4.5)$$

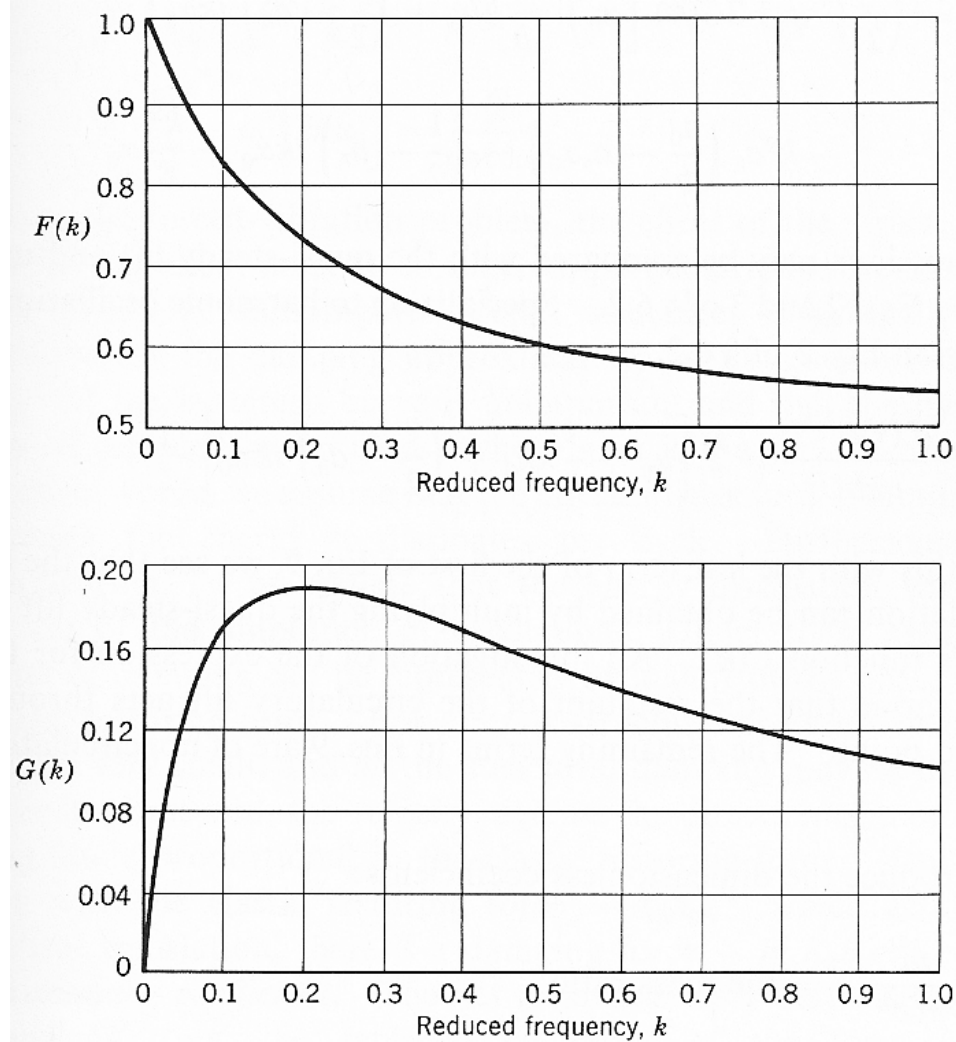


Figure 4.4: The real and imaginary parts of Theodorsen's function, $F(k)$ and $G(k)$ respectively [22]

and $\phi(s)$ is the Wagner lift deficiency function. One approximation to the Wagner function is by Jones and is highly accurate for intermediate values of s [23]

$$\phi(s) = 1 - A_1 \exp(-b_1 s) - A_2 \exp(-b_2 s) \quad (4.6)$$

where $A_1 = 0.165$, $A_2 = 0.335$, $b_1 = 0.0455$, and $b_2 = 0.3$. Given the indicial response, with Jones's approximation to the Wagner function, Duhamel's convolution integral [23] can be used to get the overall lift response to an arbitrary forcing function, $\alpha(t)$.

$$C_L(t) = C_{L\alpha} \left[\alpha(0) + \int_0^t \frac{d}{d\tau} \alpha(\tau) \phi\left(\frac{U}{b}(t - \tau)\right) d\tau \right] \quad (4.7)$$

For the analytical model, it is desirable to have the unsteady terms in a state-space form as presented in Eqn. 4.8.

$$\begin{aligned} \begin{Bmatrix} \dot{X}_1 \\ \dot{X}_2 \end{Bmatrix} &= \mathbf{A} \begin{Bmatrix} X_1 \\ X_2 \end{Bmatrix} + \begin{bmatrix} 1 \\ 1 \end{bmatrix} \alpha(t) \\ C_L &= \mathbf{C} \begin{Bmatrix} X_1 \\ X_2 \end{Bmatrix} + \mathbf{D} \alpha(t) \end{aligned} \quad (4.8)$$

To find this state-space representation, the Laplace transforms of Eqns. 4.7 and 4.8 were taken and are shown in Eqns. 4.9 and 4.10 where p is the Laplace variable.

$$\frac{C_L(p)}{C_{L\alpha}} = \alpha(p) \left[\frac{1}{2} + \frac{A_1 b_1}{p + b_1} + \frac{A_2 b_2}{p + b_2} \right] \quad (4.9)$$

$$\begin{aligned}
pX(p) &= \mathbf{A}X(p) + \begin{pmatrix} 1 \\ 1 \end{pmatrix} \alpha(p) \\
C_L(p) &= \mathbf{C}X(p) + \mathbf{D}\alpha(p)
\end{aligned} \tag{4.10}$$

These equations can then be equated to solve for the elements of the matrices of \mathbf{A} , \mathbf{C} , and \mathbf{D} in the equations for the unsteady circulatory lift per unit span:

$$\begin{aligned}
\begin{Bmatrix} \dot{X}_1 \\ \dot{X}_2 \end{Bmatrix} &= \begin{bmatrix} -b_1 \frac{U}{b} & 0 \\ 0 & -b_2 \frac{U}{b} \end{bmatrix} \begin{Bmatrix} X_1 \\ X_2 \end{Bmatrix} + \begin{bmatrix} 1 \\ 1 \end{bmatrix} \alpha(t) \\
L_c' &= \rho U^2 b C_{L\alpha} \left(\frac{U}{b} \begin{bmatrix} A_1 b_1 & A_2 b_2 \end{bmatrix} \begin{Bmatrix} X_1 \\ X_2 \end{Bmatrix} \right) + \begin{bmatrix} 1 \\ 1 \end{bmatrix} \alpha(t)
\end{aligned} \tag{4.11}$$

The circulatory lift on the airfoil is affected by both the angle of attack and also by the pitch rate (rate of change of angle of attack). From thin-airfoil theory, it is known that these two can be combined by using the angle of attack at the 3/4 chord point [23]. Combining the pitching motion and the rolling motion of the wing, the angle of attack at the 3/4 chord point can be found from

$$\alpha_{\frac{3}{4}c} = \theta + \frac{1}{U} \left(y\dot{\phi} + \dot{\theta}b \left(\frac{1}{2} - a \right) \right) \tag{4.12}$$

which replaces the angle of attack term of the circulatory lift in Eqn. 4.11.

In addition to the circulatory lift on the wing, there are also aerodynamic forces on the wing due to the mass of air surrounding the wing that must be pushed out

of the way when the wing pitches or plunges up or down. These forces are called apparent mass or non-circulatory forces, and for lift can be written [24]

$$L'_{NC} = \rho\pi b^2 \left(\ddot{h} + U\dot{\theta} - ba\ddot{\theta} \right) \quad (4.13)$$

where

$$\dot{h} = y\dot{\phi} \quad (4.14)$$

and

$$\ddot{h} = y\ddot{\phi} \quad (4.15)$$

Including both the circulatory and non-circulatory terms, the total lift per unit span can be written as

$$L' = \rho U^2 b C_{L\alpha} \left(\frac{U}{b} \begin{bmatrix} A_1 b_1 & A_2 b_2 \end{bmatrix} \begin{Bmatrix} X_1 \\ X_2 \end{Bmatrix} + \frac{1}{2} \alpha_{\frac{3}{4}c}(t) \right) + \pi \rho b^2 \left(\ddot{h} + U\dot{\theta} - ba\ddot{\theta} \right) \quad (4.16)$$

The aerodynamic pitching moment includes both circulatory and non-circulatory terms just as the lift force does. The circulatory moment is due to a constant term plus the circulatory lift force acting at the aerodynamic center of the wing segments. This can be written as

$$M_C' = \frac{1}{2} \rho U^2 b^2 C_{M_0} + b \left(\frac{1}{2} + a \right) L_C' \quad (4.17)$$

The non-circulatory terms for pitching moment are [24]

$$M'_{NC} = \pi\rho b^2 \left(ba\ddot{h} + U\frac{b}{4} \left(a - \frac{1}{2} \right) \dot{\theta} - \frac{b^2}{16} \right) \quad (4.18)$$

which yields a total pitching moment per unit span of

$$\begin{aligned} M' &= \frac{1}{2}\rho U^2 b^2 C_{M_0} + b \left(\frac{1}{2} + a \right) L'_C \\ &\quad + \pi\rho b^2 \left(ba\ddot{h} + U\frac{b}{4} \left(a - \frac{1}{2} \right) \dot{\theta} - \frac{b^2}{16} \left(a^2 + \frac{1}{8} \right) \ddot{\theta} \right) \end{aligned} \quad (4.19)$$

4.2.1 Validation of Aerodynamic Model

The analytical aerodynamic model was validated by comparing the circulatory lift response to Theodorsen's function and the total lift response to experimental data by Rainey [25] of a purely pitching wing. All roll terms in the lift and unsteady equations were ignored to allow for a purely pitching system. To compare the circulatory lift to Theodorsen's function, the Laplace transform of Eqn. 4.11 was taken which gives

$$C_{L_c}(s) = C_{L_\alpha} \left(\frac{1}{2}\alpha(s) + \frac{U}{b}A_1b_1X_1(s) + \frac{U}{b}A_2b_2X_2(s) \right) \quad (4.20)$$

and

$$\begin{aligned} sX_1(s) &= -b_1\frac{U}{b}X_1(s) + \alpha(s) \\ sX_2(s) &= -b_2\frac{U}{b}X_2(s) + \alpha(s) \end{aligned} \quad (4.21)$$

Substituting the unsteady terms, X_1 and X_2 , into the lift equation and dividing by

α

$$\frac{C_{L_c}(s)}{\alpha(s)} = C_{L_\alpha} \left(\frac{1}{2} + A_1b_1\frac{U}{bs + b_1U} + A_2b_2\frac{U}{bs + b_2U} \right) \quad (4.22)$$

The Laplace transform of the non-circulatory lift, Eqn. 4.13, divided by α is shown by

$$\frac{C_{L_{NC}}(s)}{\alpha(s)} = \pi b \left(\frac{s}{U} - \frac{ba}{U^2} s^2 \right) \quad (4.23)$$

Substituting $i\omega$ for s and gathering terms to put Eqns. 4.22 and 4.23 in terms of the reduced frequency, k , the transfer function from angle of attack to lift response in terms of the reduced frequency is written as

$$\frac{C_L(i\omega)}{\alpha(i\omega)} = C_{L_\alpha} \left(\frac{1}{2} + A_1 b_1 \frac{1}{ik + b_1} + A_2 b_2 \frac{1}{ik + b_2} \right) + \pi (ik + ak^2) \quad (4.24)$$

As indicated by Fung [22], the circulatory lift portion of this function should be equivalent to Theodorsen's function when normalized by the lift curve slope. Theodorsen's function can be written as

$$C(k) = \frac{K_1(ik)}{K_0(ik) + K_1(ik)} \quad (4.25)$$

where K_0 and K_1 are the modified Bessel functions.

In Fig. 4.5, the circulatory lift portion of Eqn. 4.24 is compared to Theodorsen's function, Eqn. 4.25. The real portion matches within 2% and the imaginary within 10%. The relatively small discrepancy can be attributed to the approximation used for the Wagner function.

Experimental data on a pitching wing by Rainey [25] was used for comparison of the total lift response. The total lift response as a function of reduced frequency is plotted in Fig. 4.6 with Rainey's data being marked by an "o". The analytical model follows the experimental data trend quite well in both magnitude and phase. As the reduced frequency increases to greater than 0.4, a slight deviation occurs between the experimental data and the total lift response. However, for the experiments presented

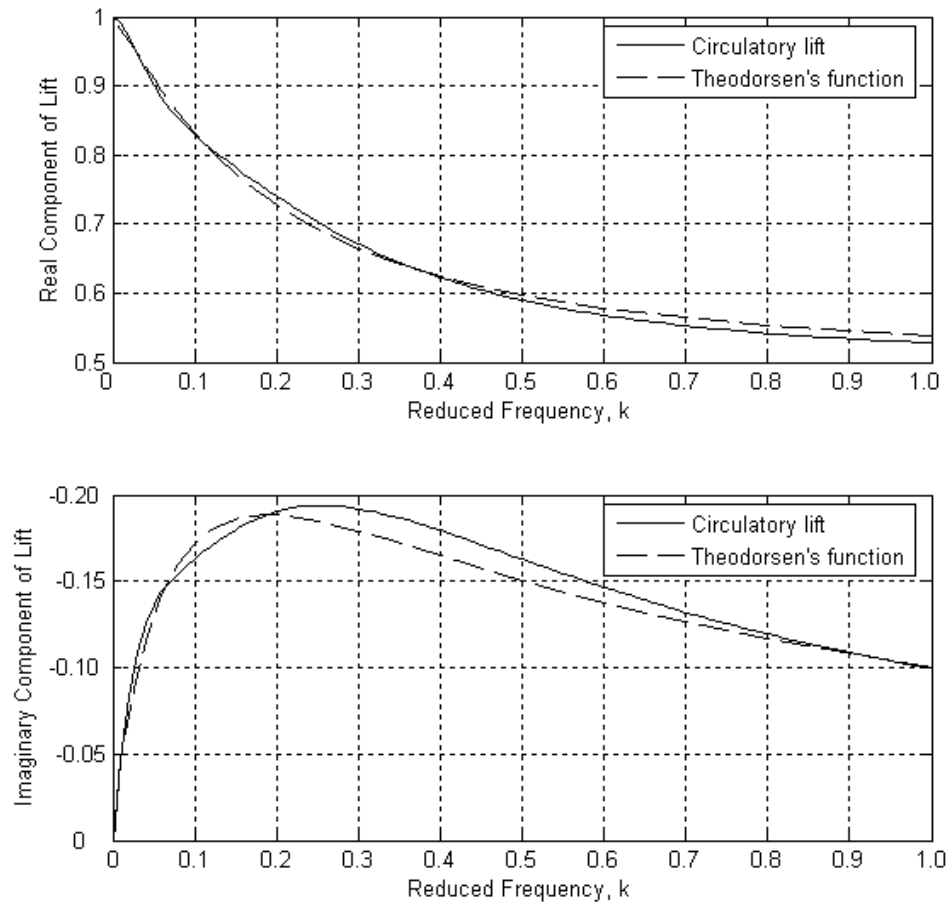


Figure 4.5: Comparison of the analytical model circulatory lift to Theodorsen's function

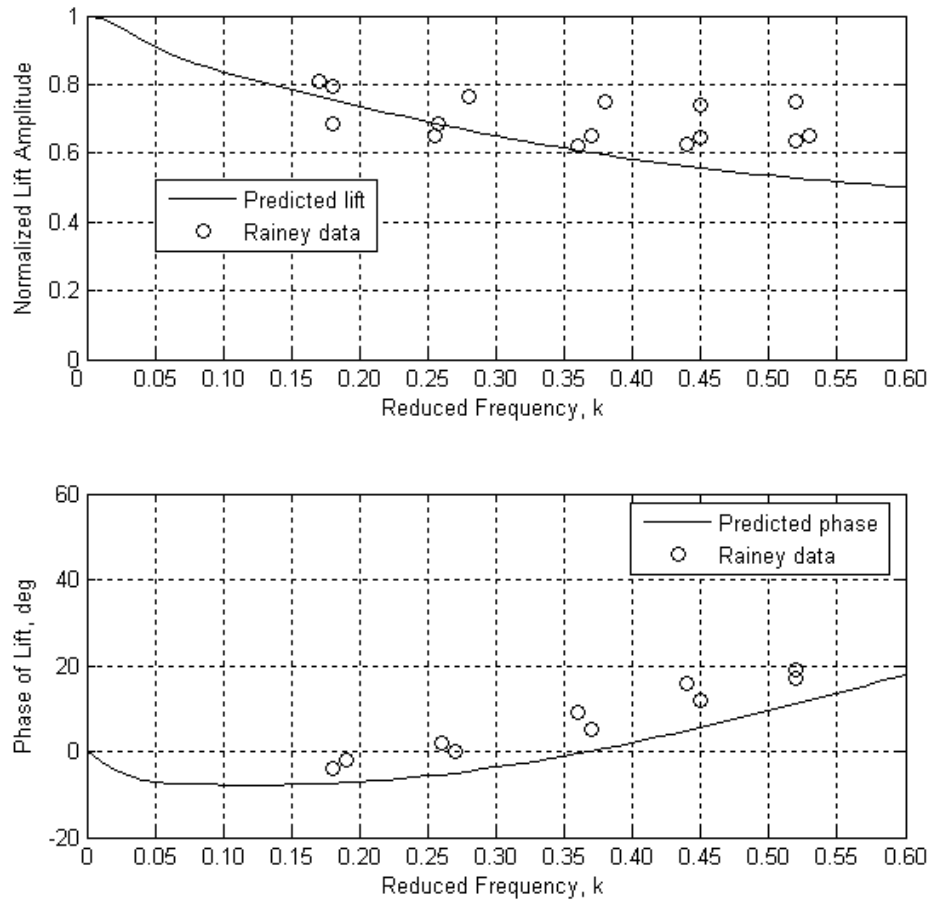


Figure 4.6: Comparison of the analytical model total lift response with pitching data from Rainey [25]

later in this thesis, the reduced frequency remained within the 0.2 to 0.3 range which matches the Rainey data nicely.

4.3 Wake Effects

Because of the trailed vortex wake system behind any lifting body, the aerodynamic lift on one airfoil segment affects all of the other nine. Consequently, to accurately predict the behavior of the segmented free wing, it was necessary to add downwash effects to the system so the effective angle of attack on each segment, including the influence of all the others, could be accurately modeled. To model the downwash, the Vortex Lattice Method (VLM) [26] was used to calculate an effective angle of attack on each segment which could then be used to determine the overall lift.

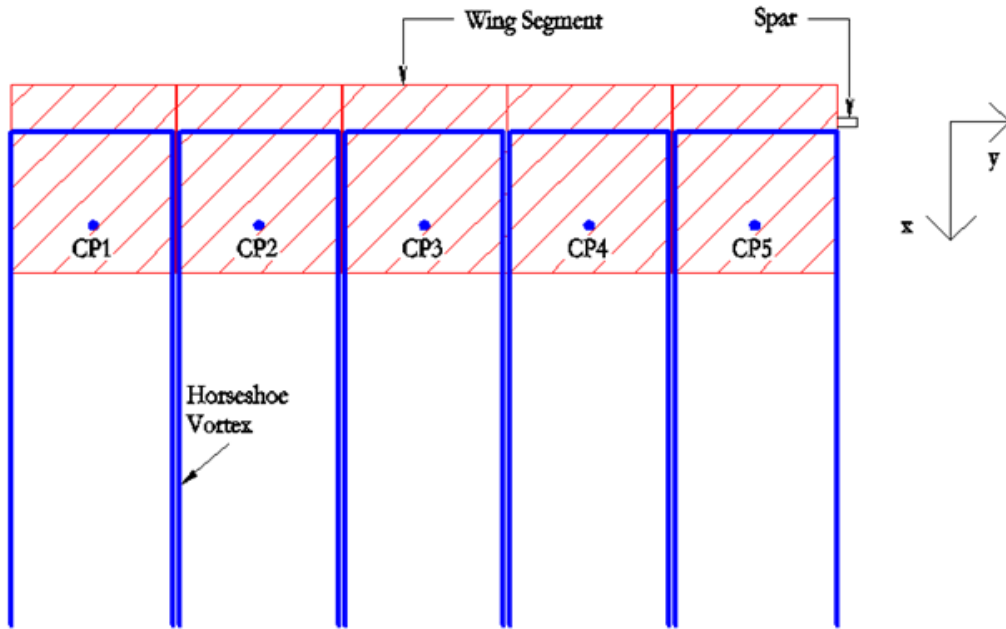


Figure 4.7: Setup of the Vortex Lattice Method on segmented free wing

Each wing segment was modeled using a set of horseshoe vortices that consisted of a bound vortex along the quarter-chord of the wing segment and two semi-infinite trailed vortices extending from the ends of the bound segment to infinity aft of the wing. Each segment had a control point placed at the three-quarter-chord centered between the two trailed vortices.

The velocity induced by a general horseshoe vortex of strength Γ_n with a length of dl is determined by use of the *law of Biot and Savart* as shown in Eqn. 4.26

$$\vec{dV} = \frac{\Gamma_n (\vec{dl} \times \vec{r}')}{4\pi r'^3} \quad (4.26)$$

Referring to Fig. 4.8, the magnitude of the induced velocity induced by a vortex filament is:

$$dV = \frac{\Gamma_n \sin \theta dl}{4\pi r^2} \quad (4.27)$$

Equation 4.27 can be integrated to obtain the total induced velocity produced by a straight vortex filament:

$$\begin{aligned} V &= \frac{\Gamma_n}{4\pi r_p} \int_{\theta_1}^{\theta_2} \sin \theta d\theta \\ &= \frac{\Gamma_n}{4\pi r_p} (\cos \theta_1 - \cos \theta_2) \end{aligned} \quad (4.28)$$

A boundary condition must be applied in order to compute the strength of the vortices where the “surface of the wing is a streamline” [26]. Since the surface behaves as a streamline, the flow does not pass through the surface of the wing but remains

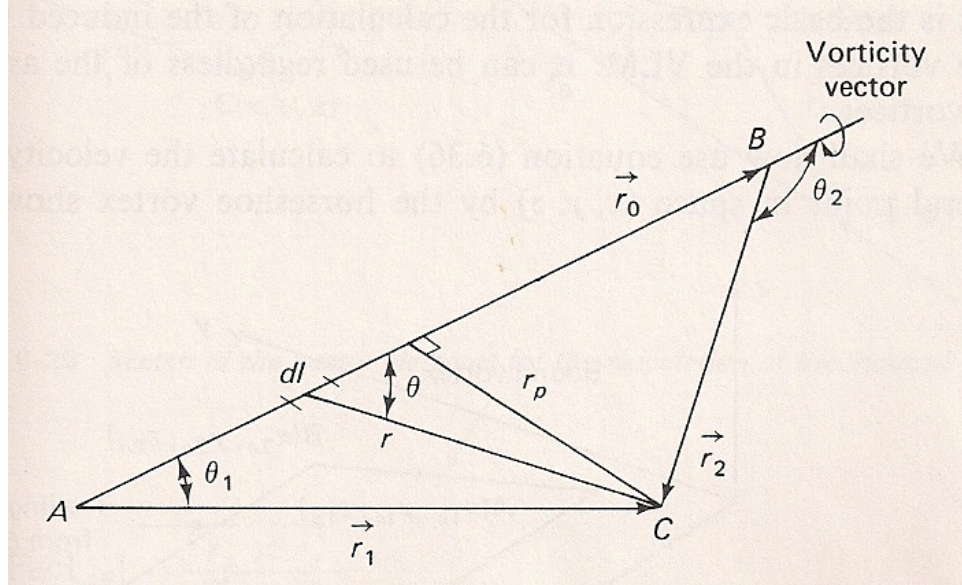


Figure 4.8: “Nomenclature for calculating the velocity induced by a finite length vortex segment” [26]

tangent to the surface. For wings with a modest slope of the mean camber line, the tangency condition can be approximated by [26]:

$$w_m - v_m \tan \phi + U_\infty \left[\alpha - \left(\frac{dz}{dx} \right)_m \right] = 0 \quad (4.29)$$

For airfoils of modest thickness, a 2-dimensional, planar approximation can be used to simplify the tangency condition to

$$w_m + U_\infty \sin \alpha = 0 \quad (4.30)$$

or for small angles of attack:

$$w_m = -U_\infty \alpha \quad (4.31)$$

The downwash at control point i from segment j can be calculated from Eqn. 4.28 and then summed to get downwash, w_{m_i}

$$w_{m_i} = \frac{1}{4\pi} \sum_j C_{ij} \Gamma_j \quad (4.32)$$

as derived in Bertin [26]. Equating this to 4.31 gives a set of equations for the vortex strengths:

$$\frac{1}{4\pi} \sum_j \mathbf{C}_{ij} \Gamma_j = -U_\infty \alpha \quad (4.33)$$

From the Kutta-Joukowski theorem [27] and the definition of the lift coefficient

$$L' = \rho U \Gamma = \frac{1}{2} \rho U^2 2b C_L \quad (4.34)$$

Solving for C_L and substituting for Γ

$$C_L = \frac{-4\pi}{b} \mathbf{C}^{-1} \alpha = C_{l_\alpha} \alpha_e \quad (4.35)$$

Finally, solving for α_e

$$\alpha_e = \frac{-4\pi}{b C_{l_\alpha}} \mathbf{C}^{-1} \alpha \quad (4.36)$$

This matrix equation provides a relationship between the angle of incidence, α , of each segment, and the aerodynamic angle of attack of the segments including the mutual influences of each segment on all the others. This effective angle of attack could then be substituted into the aerodynamic equations 4.16 and 4.19 to arrive at the total lift and moment per unit span on each segment.

4.4 Equations of Motion

By combining all the derivations from the previous sections the equations of motion for the full system were formulated. The system was set up in the following format:

$$\mathbf{C}\dot{\vec{x}} = \mathbf{A}\vec{x} \quad (4.37)$$

The state vector \vec{x} was defined as

$$\vec{x} = \left[\dot{\theta}_i \quad \theta_i \quad X_{1,i} \quad X_{2,i} \quad \dot{\phi} \quad \phi \right]^T, \text{ for } i = 1..10 \quad (4.38)$$

The superscript “T” in Eqn. 4.38 denotes the transpose of the matrix. Solving for $\dot{\vec{x}}$, the stability of the system could be analyzed by determining the eigenvalues of the matrix $C^{-1}A$. This was performed using the MATLAB program and results will be presented in the form of root-locus plots. The eigenvectors of the system matrix were used to determine the different modes of oscillation of the system.

The equations for pitch, roll, X_1 , and X_2 are shown in order in Eqs. (26-28).

Pitch:

$$\begin{aligned}
& \left(\pi \rho b^4 x a^2 + \frac{1}{8} \pi \rho b^4 x + I_{yy} \right) \ddot{\theta}_i + (-\pi \rho b^3 x a y_i - 2 m b \delta_{x_i} y_i) \ddot{\phi} = \\
& \left(\pi \rho b^3 x U \left(\frac{-1}{2} + a \right) + \frac{1}{8} \rho U b^3 x C_{l_\alpha} C_{ij} (1 - 4a^2) \right) \dot{\theta}_i \\
& + \left(\frac{1}{4} \rho U^2 b^2 x C_{l_\alpha} C_{ij} (1 + 2a) \right) \theta_i \\
& + \left(\frac{1}{2} \rho U^3 b x C_{l_\alpha} A_1 b_1 (1 + 2a) \right) X_{1,i} \\
& + \left(\frac{1}{2} \rho U^3 b x C_{l_\alpha} A_2 b_2 (1 + 2a) \right) X_{2,i} \\
& + \left(\frac{1}{4} \rho U b^2 x C_{l_\alpha} y_j C_{ij} (1 + 2a) \right) \dot{\phi}
\end{aligned} \tag{4.39}$$

Roll:

$$\begin{aligned}
& (\rho x y_i \pi b^3 a + 2 m y_i \delta_{x_i} b) \ddot{\theta}_i + (-\rho x y_i^2 \pi b^2 - I_{xx}) \ddot{\phi} = \\
& \left(\rho x y_i \pi b^2 U + \frac{1}{4} \rho x y_i U C_{l_\alpha} b^2 C_{ij} (1 - 2a) \right) \dot{\theta}_i \\
& + \left(\frac{1}{2} \rho x y_i b U^2 C_{l_\alpha} C_{ij} \right) \theta_i \\
& + (\rho x y_i U^3 C_{l_\alpha} A_1 b_1) X_{1,i} \\
& + (\rho x y_i U^3 C_{l_\alpha} A_2 b_2) X_{2,i} \\
& + \left(C + \frac{1}{2} \rho x y_i y_j U C_{l_\alpha} b C_{ij} \right) \dot{\phi} \\
& + K \phi
\end{aligned} \tag{4.40}$$

Unsteady Aerodynamic states:

$$\begin{aligned} \begin{bmatrix} \dot{X}_{1,i} \\ \dot{X}_{2,i} \end{bmatrix} &= \begin{bmatrix} \frac{-U}{b}b_1 & 0 \\ 0 & \frac{-U}{b}b_2 \end{bmatrix} \\ &+ \begin{pmatrix} 1 \\ 1 \end{pmatrix} \left[\left(\frac{b}{2U}C_{ij}(1-2a) \right) \dot{\theta}_i + C_{ij}\theta_i + \left(\frac{y_j}{U}C_{ij} \right) \dot{\phi} \right] \end{aligned} \quad (4.41)$$

Combining all of these equations produces a set of 42 coupled first-order differential equations, 10 for $\ddot{\theta}$, 10 for $\dot{\theta}$, 10 for \dot{X}_1 , 10 for \dot{X}_2 , one for $\ddot{\phi}$, and one for $\dot{\phi}$. The equations for $\dot{\theta}$ and $\dot{\phi}$ are trivial and of the form $\dot{\theta} = \dot{\theta}$ and $\dot{\phi} = \dot{\phi}$.

4.5 Wind Tunnel Model

The center of gravity position was located on the spanwise axis of rotation. The analytical model used for the wind tunnel model was substantially the same as used for the truck model. The input parameters were changed to match the geometry of the smaller model. In addition, two new friction terms were added to the model to account for friction in the pitch and roll bearings. These friction terms were added to the equations of motion (Eqns. 4.1 and 4.2) as presented in Eqn. 4.42.

$$\begin{aligned} M_y &= M_{AERO} + my_i\delta_{x_i}\ddot{\phi} - \mu_{k_{pitch}}\dot{\theta} \\ M_x &= -\sum_i L_i y_i - K\phi - C\dot{\phi} + \sum_i my_i\delta_{x_i}\ddot{\theta}_i - \mu_{k_{roll}}\dot{\phi} \end{aligned} \quad (4.42)$$

CHAPTER 5

RESULTS

5.1 Initial Wind Tunnel Test

An initial wind tunnel model was tested as both a proof of concept and then as a verification of the computer model. The first experimental test on the wind tunnel model was to determine the rolling moment generated by the model as a result of spanwise flow variations created by an upstream vortex-generating oscillating wing. However, during the first tests, the wind tunnel model began to have a destructive oscillation about the rolling axis. The test was immediately terminated. It was assumed that play in the mount and imbalance of the wing segments were responsible for the oscillation.

After a new mount was constructed for the model and the segments were balanced about their hinge axis, the rolling moment generated by the spanwise flow variation over the model was measured. For each of the three configurations, the rolling moment was measured with the vortex-generating wing at full positive and full negative deflection. The difference between the two rolling moments gives an indication of the amount of aerodynamic load that would be transmitted to the aircraft structure. This simulates the aircraft encountering a gust that varies across the span of the wing. The results of the wind tunnel tests are shown in Table 5.1.

As seen in Table 5.1, the single free-wing transfers a load of 1.2 ft-lbs to the fuselage of the model. However, when each wing half is allowed to move freely from the

	Single Freewing	Left/Right Freewing	Segmented Freewing
Rolling Moment	1.175 ft-lbs	0.838 ft-lbs	0.428 ft-lbs
Reduction in Rolling Moment		(29%)	(64%)

Table 5.1: Rolling moments of three configurations

other, nearly a 30% reduction in the transferred load occurs. This is even further enhanced by the segmented free wing which reduces the transmitted load from the wings to the fuselage by 64%. These results, although preliminary, show strong evidence that the segmented free-wing design would successfully reduce the gust response of HALE aircraft as they pass through the troposphere.

5.2 Experimental Model

Following the success of the initial wind tunnel model, a larger wing was constructed as described in Section 3.1. The experimental testing of this model was performed by attaching the rig to a full size pickup truck and slowly increasing the speed of the system while observing the results. Digital videos of the tests were acquired and used to estimate oscillation frequencies and onset velocities.

At a velocity of approximately 22 ft/s an unstable oscillatory rolling motion occurred during experimental testing. As speed was increased the frequency stayed the same but the amplitude increased dramatically. The system had an oscillation frequency of approximately 1.2 Hz with a maximum rolling angle of about 10 degrees before the speed was reduced. Reference [3] found a divergent spiral mode in their computational analysis of a free-wing aircraft with independent left and right wing panels. It is conjectured that this spiral mode is appearing as an unstable oscillatory

roll mode in this experimental apparatus due to the mechanical restraints of the rolling motion.

Several possible solutions to the unstable motion were examined including increasing the rolling moment of inertia, changing the center of gravity of the wing segments, and changing the number of segments with results shown in Table 5.2. To increase the rolling moment of inertia, aluminum pipes were attached to the wingtips extending beyond the wingtips by two feet. This method provided very little damping to the system and was deemed unsuccessful. The second test consisted of changing the center of gravity of the segments by adding weight to the counterweight extending out beyond the leading edge of each segment. This also proved unsuccessful. Reducing the number of segments increased the speed at which the unstable mode occurred, but did not eliminate it.

As an additional test, the mounting system for the wing was modified to allow the wing to roll freely as it would on a flying aircraft. Once the mechanical roll restraint was removed the oscillation was gone, however as anticipated, a divergent mode took its place. The system would consistently roll at very low speeds, which would be expected to be the unstable spiral mode. The system was very hard to control and could never be trimmed.

With the initial simple modifications to the experimental system proving unsuccessful, the design was modified to allow for the attachment of fixed segments on each wingtip. This design change allowed for various sizes of fixed segments to be attached ranging from as six inches wide to two feet wide. It was hoped that the fixed segments would provide adequate damping to stabilize the system.

The fixed segments were a different design than the free-wing segments. The chord length of the fixed segments was the same as the free-wing segments, however, the span of the segment varied. Fixed segments of four different sizes were made;

Experimental Runs		
System	Configuration	Result
Mechanically Restrained	Standard	Unstable oscillation at approx. 22 ft/s
	Increased Rolling Inertia	Unstable oscillation at approx. 22 ft/s
	CG Position	Unstable oscillation at approx. 22 ft/s
	Decreased number of Segments	Unstable oscillation at approx. 22 ft/s
	Fixed Segments	Stable at all tested velocities
Mechanically Free-to-Roll	Standard	Unstable roll at all velocities
	Fixed Segments	Neutrally Stable for all velocities

Table 5.2: Results of the experimental testing on the segmented free wing

24, 18, 12, and 6 inches in span. The airfoil for the fixed segments was a symmetric NACA 0012 airfoil so the only lifting force would be from the free-wing segments. Additionally, the spar was placed at the quarter-chord to minimize the moment of the fixed segments. The segments were placed at zero angle of attack.

The experimental platform with fixed-segments was tested first in the mechanically restrained roll setup. The 24 inch segment was the first fixed segment tested during the experiment. With the fixed segments attached to the platform, the system demonstrated a drastic increase in stability. The system no longer had the catastrophic divergent rolling oscillation that was seen in previous experimental attempts. The platform remained straight and level throughout a large range of velocities with a maximum sustained velocity of 66 *ft/s*. A dihedral formed in the wings due to the lift being produced by the free-wing segments. Very little movement occurred in the segments once equilibrium of the system was reached.

Testing continued with each of the other fixed segment sizes. Mechanically restrained in roll, the experimental platform was able to demonstrate satisfactory stability using all sizes fixed segments, including the 6 inch segment. All segment sizes tested appeared to be sufficient to provide dynamic stability to the experimental platform.

In the next series of tests, the wing was allowed to roll freely with the fixed segments attached to the tips. Using the 24 inch segments, the wing did not behave as it had without the fixed segments. The free wing did not roll to one side or the other as had been seen before. In order to keep the free wing level, some mechanical control was required by the transmitter from the cab. The system did not damp itself out, but the instability did not grow either. As the size of the fixed segments decreased, the sensitivity of the segmented free wing to a disturbance grew and the pilot controlling the wings had more trouble holding the wings straight and level.



Figure 5.1: Segmented free wing with fixed segments attached to the tip flying with a visible dihedral

Although difficult, it was possible to trim the wing with the 6 inch segments. It was much easier to maintain trimmed flight of the segmented free wing with the 24 inch segments as they were not as sensitive to disturbances.

When the system was flown without the fixed segments, the segmented free wing was dynamically unstable in both the mechanically restrained and mechanically free states. However, when the fixed segments were attached to the tips of the experimental platform the system demonstrated strong dynamic stability in the mechanically restrained state. Any perturbations were quickly damped out and steady flight was quickly achieved for all fixed segment sizes. In the mechanically free state, the segmented free wing appeared to be neutrally stable. There appeared to be no damping or divergence in the system resulting from any perturbations.

5.3 Analytical Modeling

An eigen analysis was performed to study the dynamic stability properties of the segmented free-wing equations of motion. The goals of this analysis were to understand the nature of the instability, to facilitate predicting its onset, and to find methods for eliminating it. The analytical model was able to successfully predict the oscillation in the mechanically restrained state and the instability in the mechanically free state, both without the fixed segments. With the addition of the fixed segments in the computer model the mechanically restrained system became dynamically stable as was seen in the experimentation. The analytical model also predicts neutrally stable dynamic system in the mechanically free state.

5.3.1 System Properties

In order to analyze the system, the mass properties of the wing and elastic properties of the mount were needed. The mass moments of inertia, I_{xx} and I_{yy} , were initially estimated based on approximations of the geometry. After the mass moments of inertia were estimated, they were tested experimentally using a bifilar pendulum as pictured in Fig 5.2. To obtain the estimated rolling moment of inertia, the system was modeled as a rectangular parallelepiped with dimensions of 13.3 feet in span, 16 inch chord, and approximately 3 inches thick. The entire system was weighed to obtain its mass in slugs and the rolling moment of inertia, I_{xx} , was calculated using Eqn. 5.1 [28].

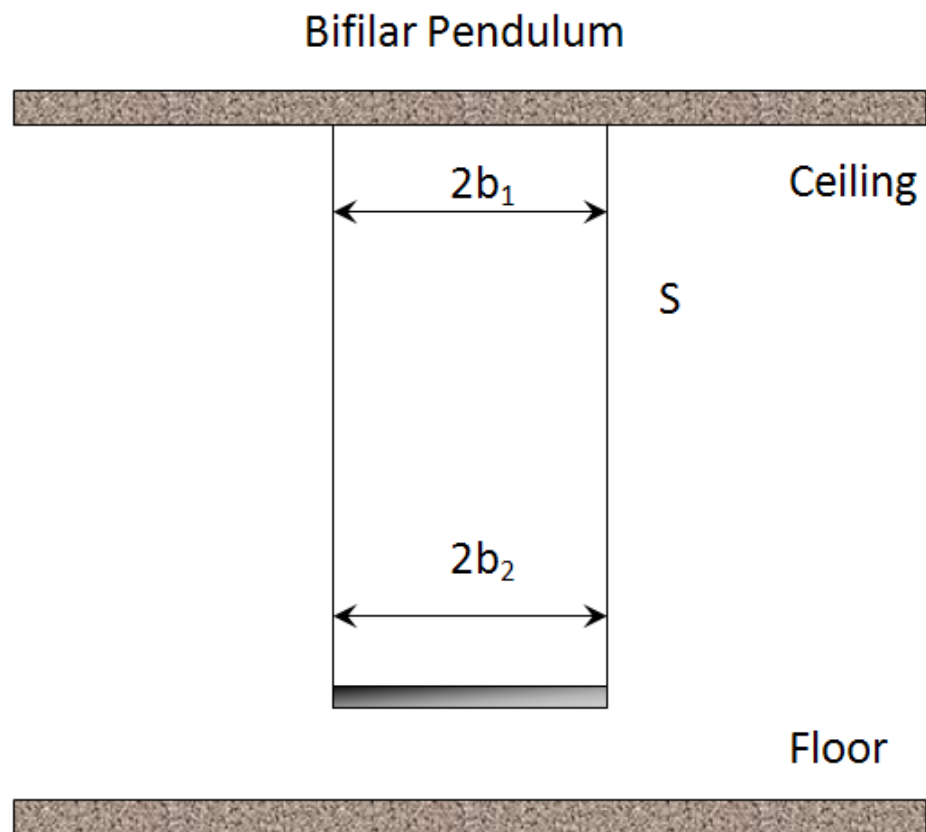


Figure 5.2: Diagram of the bifilar pendulum setup

$$I_{xx} = \frac{1}{12}m(\text{span}^2 + \text{thickness}^2) \quad (5.1)$$

Using AutoCAD 2004, the airfoil shape was drawn and the polar area moment of inertia was calculated. Knowing the density and the span of the wing segment, the estimated pitching mass moment of inertia was calculated. In addition to the wing segment, the counterweight extending beyond the leading edge of the wing was treated as a point mass and its moments of inertia added accordingly.

$$I_{yy} = J_y x \rho_{seg} + l^2 m_{cw} \quad (5.2)$$

The bifilar pendulum was then used to experimentally obtain the mass moments of inertia. The experimental values were compared to the estimated values to determine validity of the experimental value. To maintain simplicity of the experimental model, nonlinear aerodynamic damping was ignored and the moment of inertia was calculated using Eqns. 5.3 and 5.4 [29].

$$k^2 = \frac{gT^2}{4\pi^2} \left(\frac{b_1 b_2}{Y} \right) = \frac{gT^2}{4\pi^2} \frac{b_1 b_2}{[S^2 - (b_2 - b_1)^2]^{1/2}} \quad (5.3)$$

$$I = Mk^2 = \frac{MgT^2}{4\pi^2} \frac{b_1 b_2}{[S^2 - (b_2 - b_1)^2]^{1/2}} \quad (5.4)$$

The length of the two strings are denoted by S and are at equal angles from the vertical. The distance between the two points of suspension and the distance between the mounting points are denoted by $2b_1$ and $2b_2$ respectively. The perpendicular distance between the suspension point and the mounting point is represented by Y . T is the period of oscillation and M is the mass of the system. Finally, I is the moment of inertia about the vertical axis and k is the radius of gyration. Figures 5.3

and 5.4 show the experimental model and the single wing segment mounted on the bifilar pendulum and Auburn University's Adaptive Aerostructures Lab.

The spring force in the experimental mounting beam was calculated using the angle of twist equation and solving for the torque [30].

$$T = \frac{JG}{L}\phi \quad (5.5)$$

where

$$K = \frac{JG}{L} \quad (5.6)$$

The mounting beam was fabricated from standard dimensional lumber by laminating two 20' long nominally 2" x 4" (1 1/2" x 3 1/2" actual dimension) pieces of wood stock. The spring force is highly dependent on the species of wood used to make the mounting beam. The spring force varies 400 *ft - lbs/rad* within just a species family. Unfortunately, the exact species of wood was unknown, but it was assumed to be from the Pine family. Using the material properties of Lodgepole Pine shown in Table 5.3 [31], a modulus of rigidity could be calculated for the radial tangential plane of the lumber. A diagram of the axis configuration is shown in Fig. 5.5. The modulus of rigidity, G , was calculated to be 964,800 psf. The estimated modulus of rigidity was used in the spring constant equation and an estimated value of K was calculated to be 123.6 *ft - lbs/rad*. No simple analysis for the damping coefficient, C , was available, so for this initial study the value was assumed to be negligible compared to the aerodynamic forces on the wing system.

To obtain a more accurate value of K , the spring force of the beam was experimentally determined by applying a torsional loading to the mounting beam about



Figure 5.3: Experimental model mounted on the bifilar pendulum in Auburn University's Adaptive Aerostructures Lab

G_{RT}/E_L	E_L (lb/in ²)
0.005	1.93E+06

Table 5.3: Lodgepole Pine elastic properties

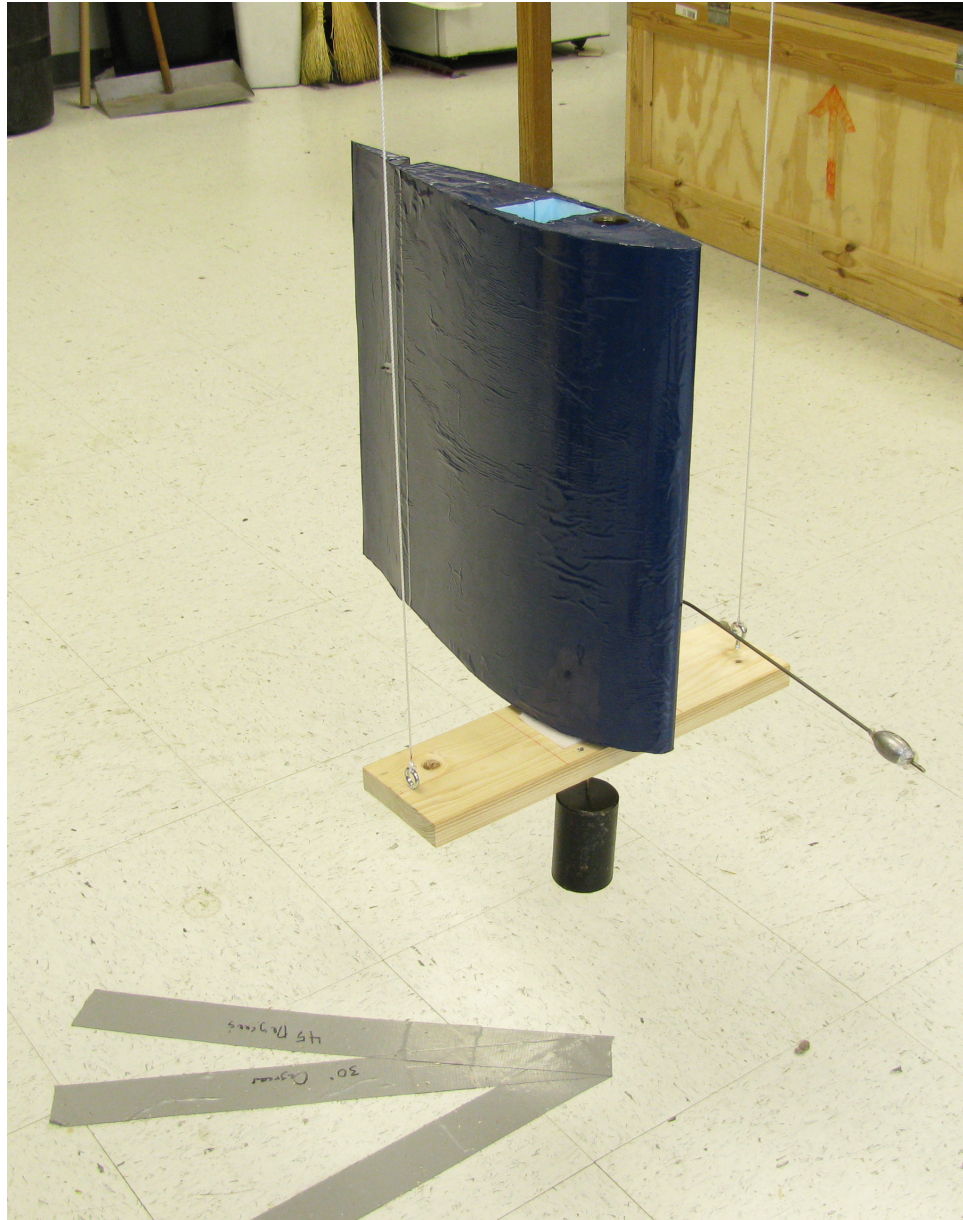


Figure 5.4: Experimental segment mounted on the bifilar pendulum in Auburn University's Adaptive Aerostructures Lab

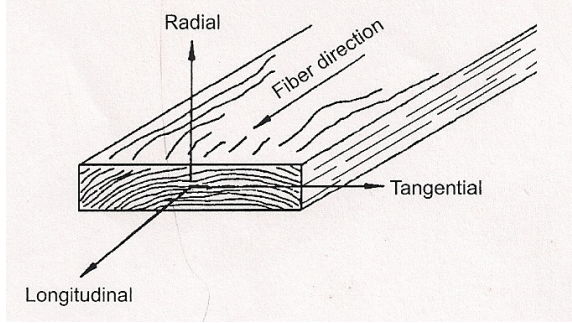


Figure 5.5: Axis orientation for modulus calculations [31]

the longitudinal axis. The spring force was measured by twisting the beam to a pre-determined angle and taking a measurement of the applied torque required to achieve the angle. The beam was twisted to 5, 10 and 15 degrees with several torque readings at each angle to obtain an adequate average. From the torque measurements, K was calculated by dividing the measurement by the respective angle of twist. The experimental results yielded an average K value of $482.5 \text{ ft} - \text{lbs}/\text{rad}$ and are shown in Table 5.4.

Twist Angle (deg)	Torque (ft-lbs)							Avg.	K
	5	40	45	38	45	45	40		
10	80	85	95	80	-	-	-	85.0	487.0
15	135	130	125	120	120	120	-	125.0	477.5
								K Avg. = 482.5	

Table 5.4: Data from spring constant test on mounting beam

5.3.2 Analytical Model Without Fixed Segments

The root locus plot in Fig. 5.6 shows the different modes of the restrained segmented free wing. The first eigenvalue is denoted by a circle and then the subsequent eigenvalues are denoted by a plus sign. Ten stable pitching modes can easily be seen labeled in Fig. 5.6 forming a fan shape originating at zero. The scatter in the pitching

mode is due to the wake effects of each wing segment upon the other. There are two rolling modes associated with the mechanically restrained system. One of the modes is stable and is labeled in Fig. 5.6. The second mode is the unstable rolling mode that was seen in the experimental testing of the segmented free wing.

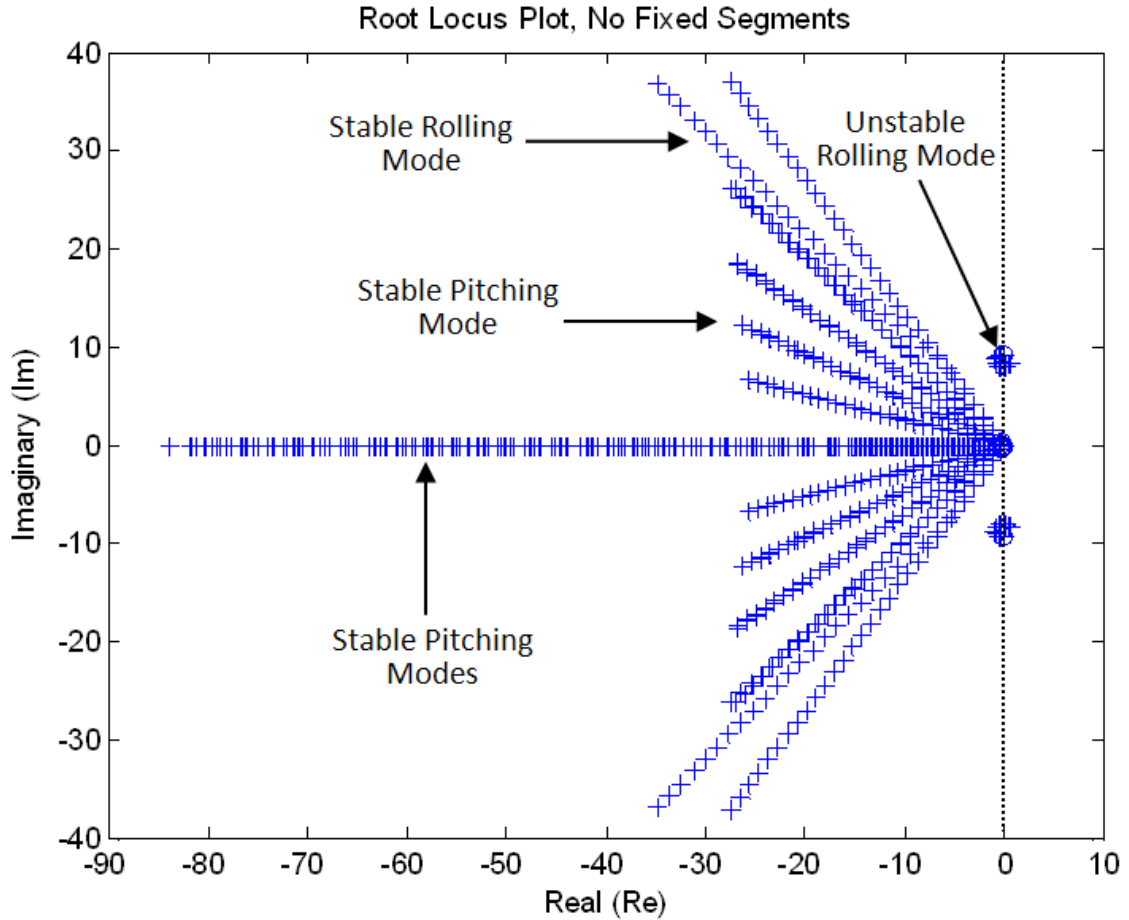


Figure 5.6: Root locus plot of the full aerodynamic model for the mechanically restrained model without fixed segments

The analytical model velocity was steadily increased from one foot per second to 150 *ft/s* by 0.1 *ft/s* intervals. With a velocity of 150 *ft/s* the analytical model predicts the segmented free wing will be unstable with an oscillation frequency of 1.31 Hz. This frequency is within 10% of the experimental frequency of 1.2 Hz. The

analytical model shows that as the velocity is increased, the frequency remains the same but the real part of the unstable root becomes increasingly positive. Figure 5.7 shows a zoomed view of the root locus plot for the full aerodynamic model that is mechanically restrained in roll without the fixed segments attached. In Fig. 5.7 it is easy to see the small changes in the unstable mode as the velocity is increased.

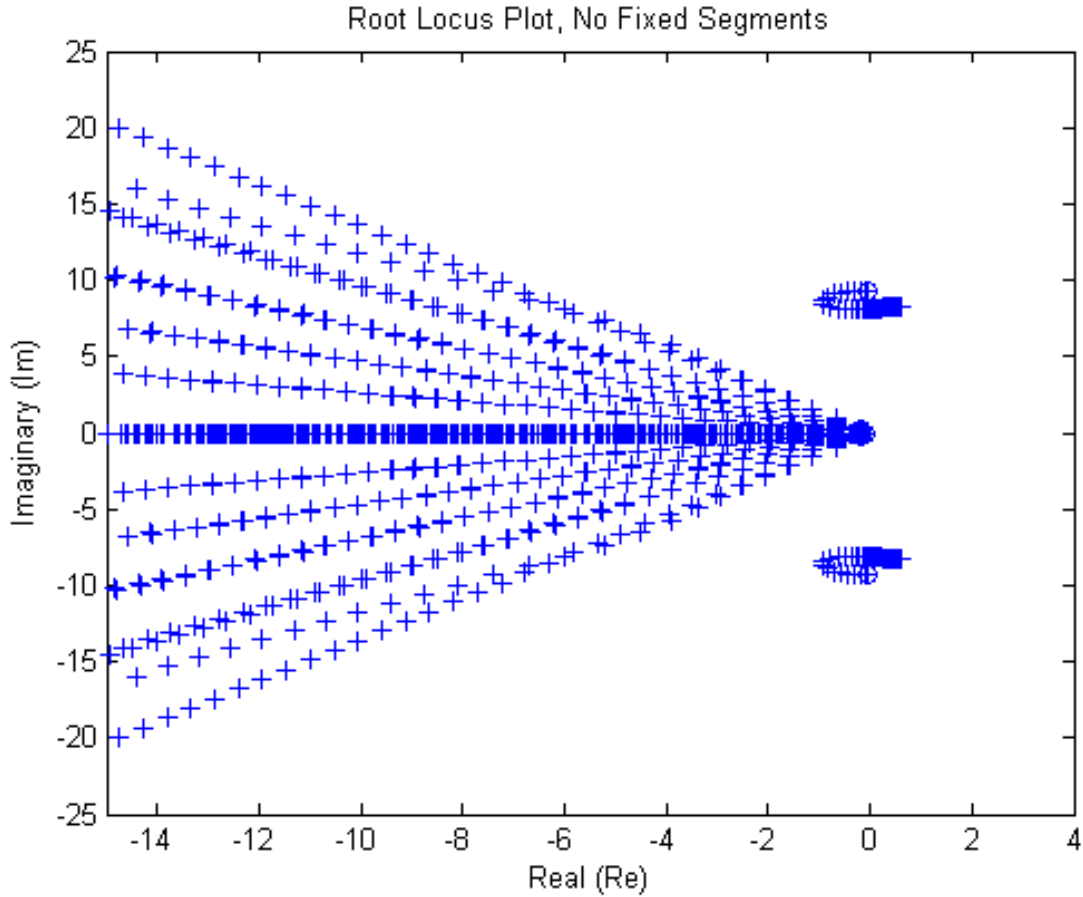


Figure 5.7: Root locus plot of the full aerodynamic model for the mechanically restrained model without fixed segments from a zoomed in perspective

Mechanically freeing the roll in the analytical model produces a result that is both expected and agrees with previous studies conducted by Porter and Brown [3]. The analytical model predicts an unstable roll mode that grows in magnitude with

the increase in velocity. The positive real root can be seen in Fig. 5.8. All the same modes occur as in the mechanically restrained system except the unstable oscillating rolling mode has now become an unstable rolling mode. This unstable rolling mode is analogous to the unstable spiral mode reported in Ref. [3]. The unstable roll mode is even more visible when looking at the locus plot zoomed in about the origin as in Fig. 5.9

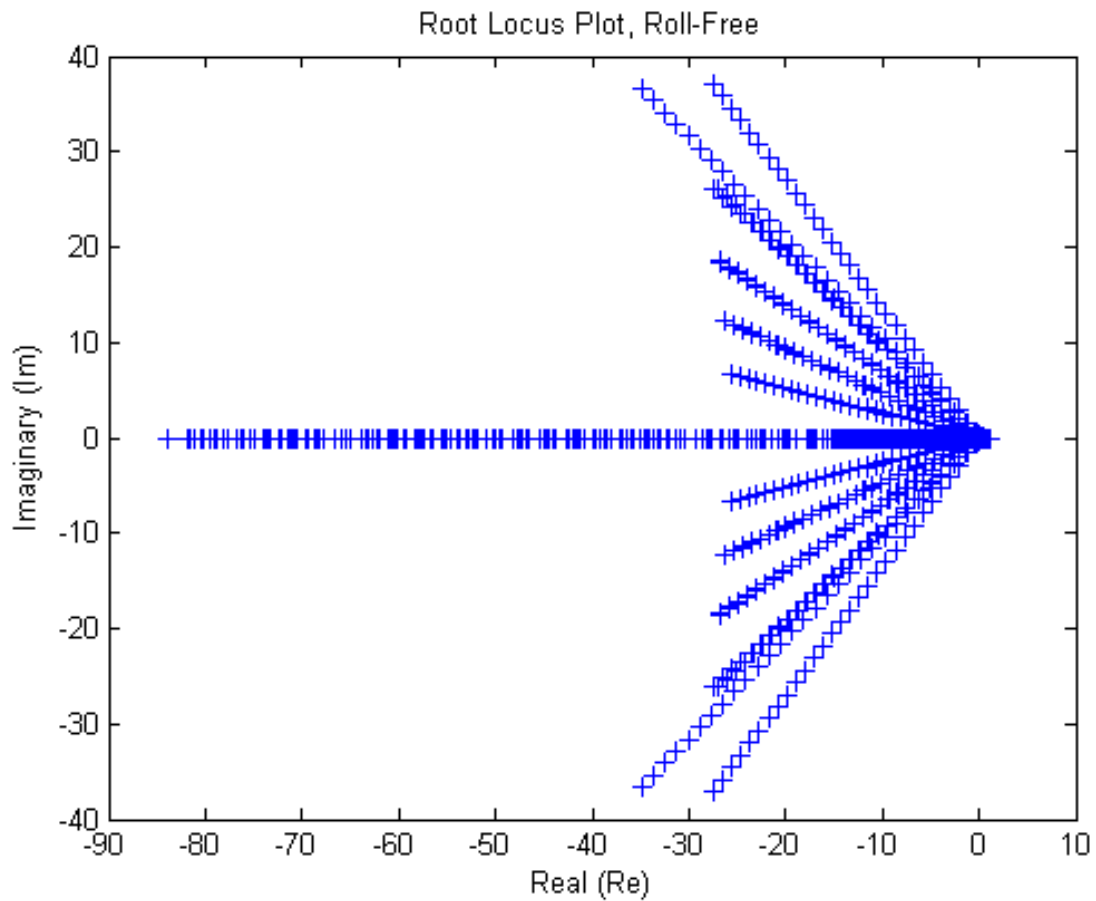


Figure 5.8: Root locus plot for the full aerodynamic model for the system mechanically free in roll without fixed segments

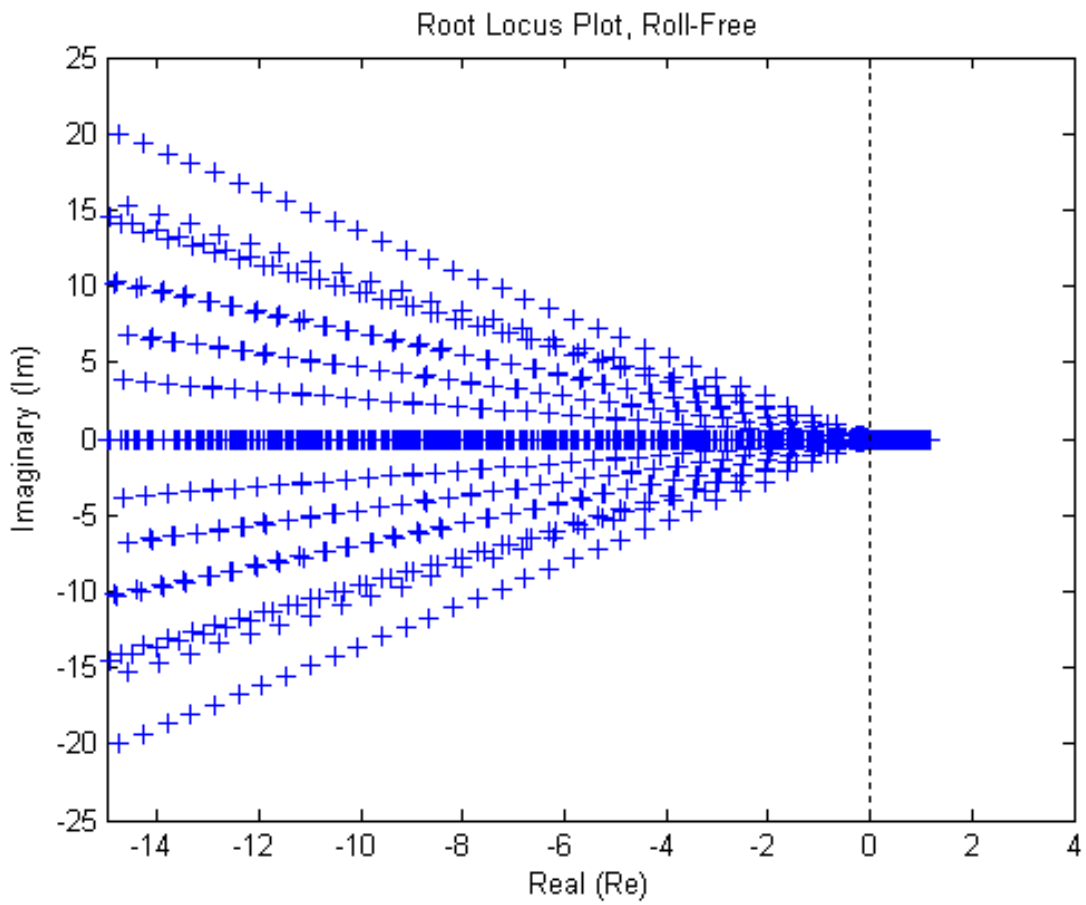


Figure 5.9: Root locus plot for the full aerodynamic model for the system mechanically free in roll without fixed segments zoomed in about the origin

5.3.3 Analytical Model With Fixed Segments

Adding fixed segments to the analytical model produces a dynamic stability that matches the experimental results. When adding fixed segments to the analytical model placed at the wingtips of the segmented free wing, the analytical model predicts a dynamically stable system. The root locus plot of the full aerodynamic model, restrained in roll, and with fixed segments attached, is presented in Fig. 5.10 and shows the newly stable rolling mode becoming increasing stable as velocity increases. All the modes from the previous root locus plot of the same system setup are present and exhibit the same behavior. The previously stable rolling mode has the same shape, however, it is more heavily damped with the fixed segments attached to the segmented free wing. Zooming into the origin, the behavior of the newly stable rolling mode can easily be seen. Figure 5.11 clearly shows the stable rolling mode becoming increasingly damped as the velocity is increased. Also, as the velocity is increased the oscillation frequency of the stable rolling mode remains almost constant.

The free-to-roll system contains an unstable roll mode in the analytical model when the fixed segments are not attached to the wingtips of the segmented free wing. Adding the fixed segments to the analytical model for the free-to-roll system produces a system that is no longer unstable. However, with the addition of the fixed segments, several zero eigenvalues appear. Instead of being dynamically unstable, the analytical model predicts a neutrally stable system. This would agree with experimental results where the segmented free wing could be trimmed, but if a perturbation entered the system there was no damping. Figure 5.12 shows the root locus plot for the roll-free system with the fixed segments attached. Figure 5.13 is the same plot but zoomed in about the origin.

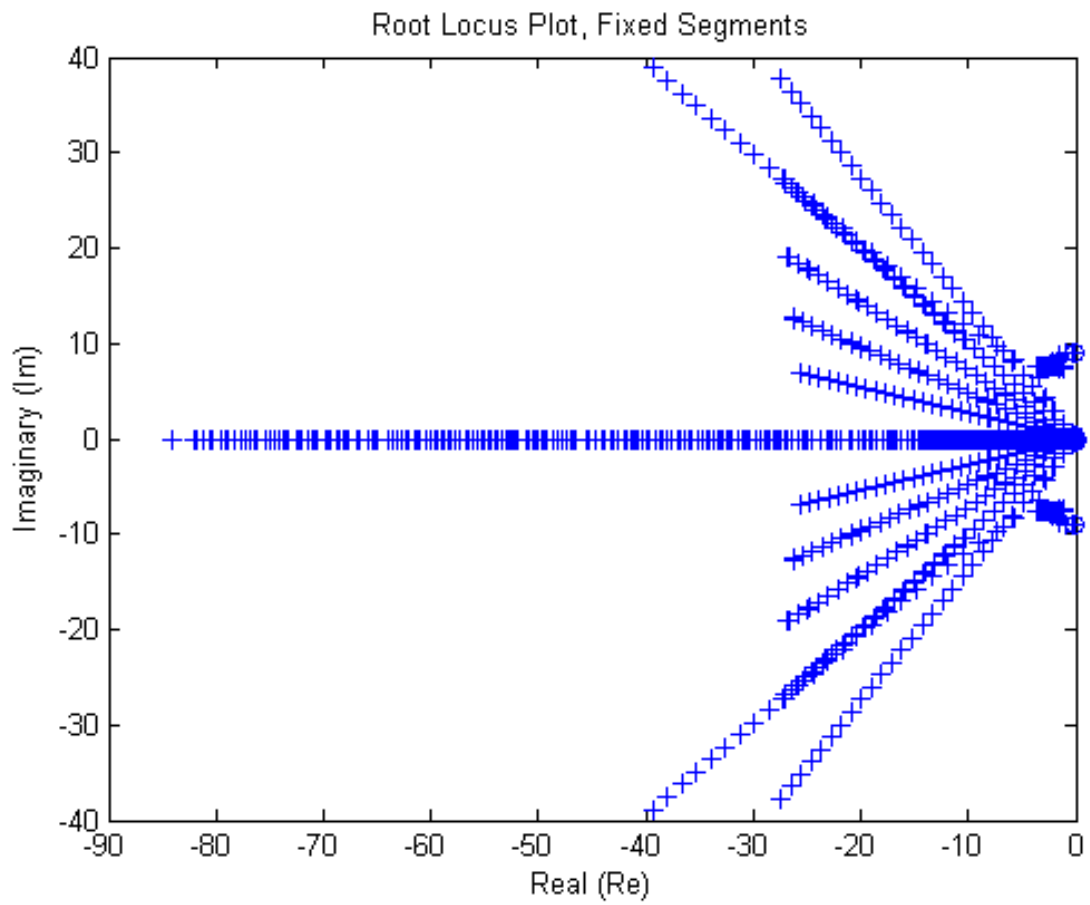


Figure 5.10: Root locus plot for the full aerodynamic model for the system mechanically restrained in roll with fixed segments

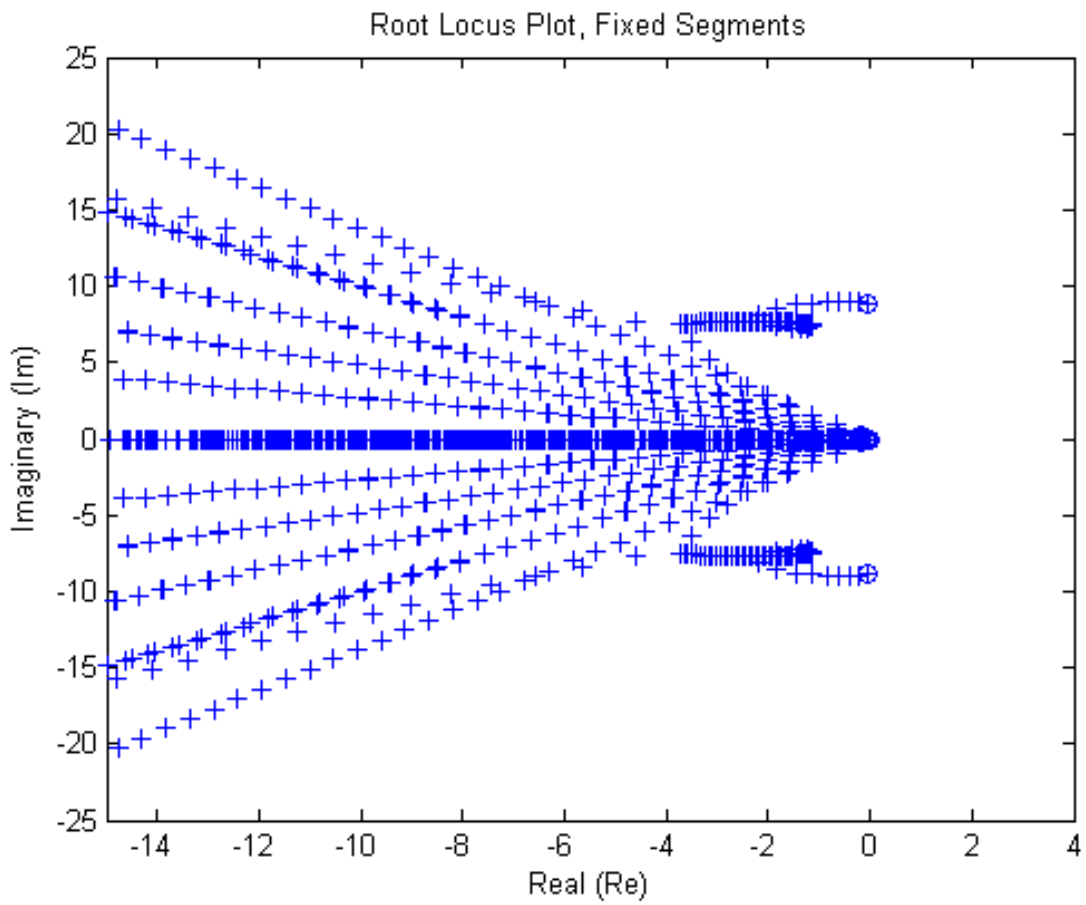


Figure 5.11: Root locus plot for the full aerodynamic model for the system mechanically restrained in roll with fixed segments attached, zoomed about the origin

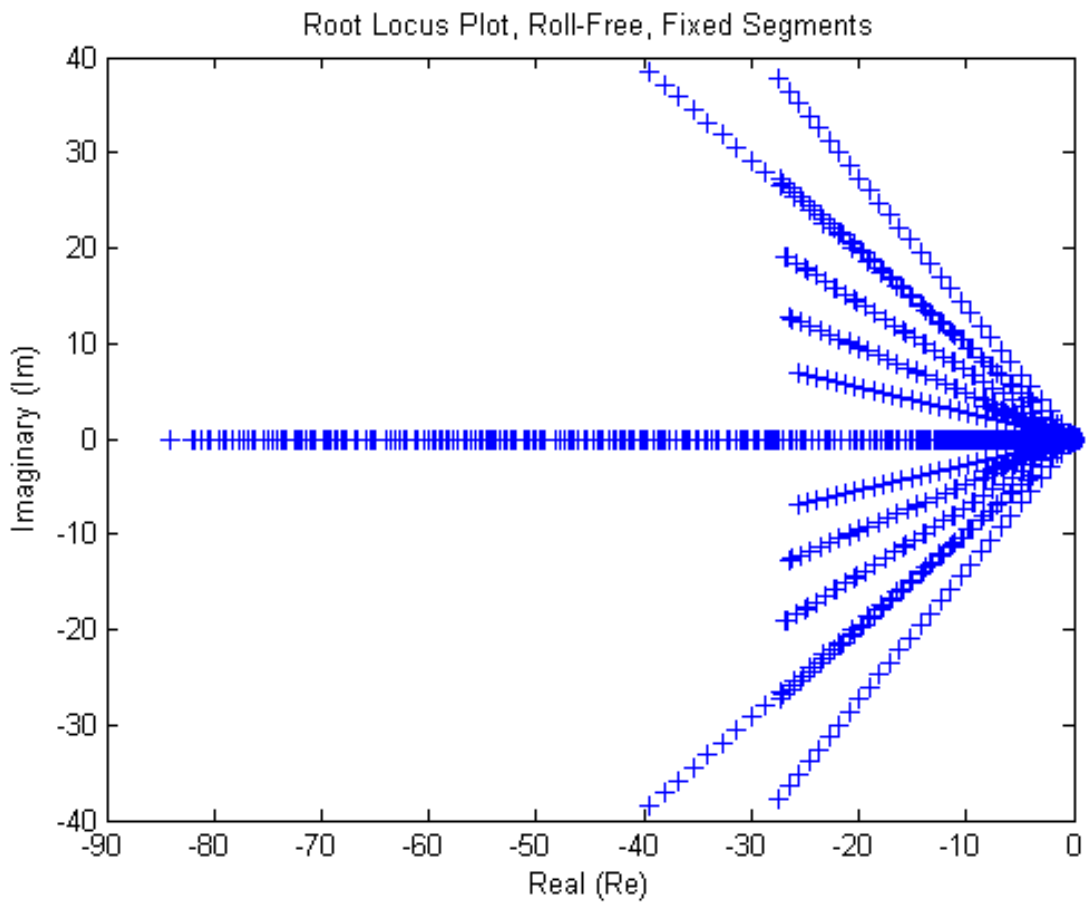


Figure 5.12: Root locus plot for the full aerodynamic model for the system mechanically free in roll with fixed segments attached

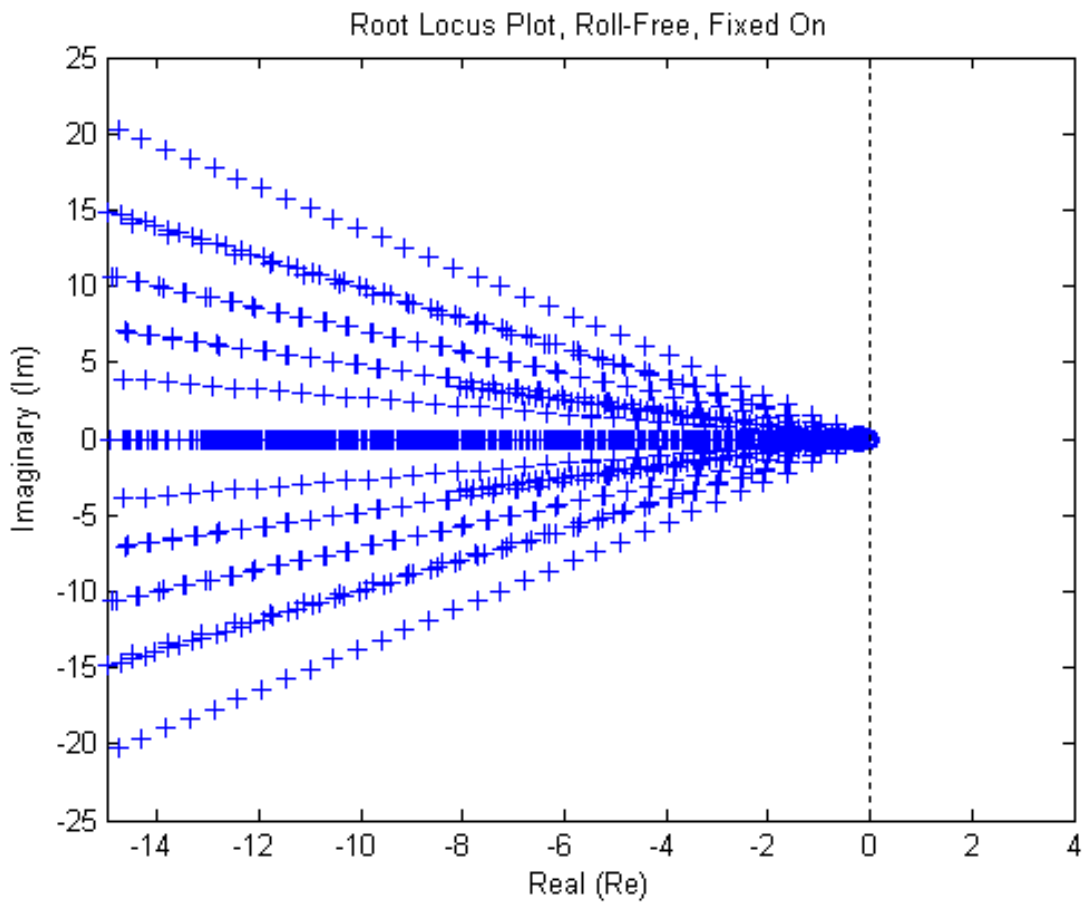


Figure 5.13: Root locus plot for the full aerodynamic model for the system mechanically free in roll with fixed segments attached, zoomed in about the origin

5.3.4 Analytical Model Compared to Experimental Results

The analytical model predicts a crossover velocity, the velocity at which the system becomes dynamically unstable, of 49.5 ft/s (33.8 mph). In the experimental results, the velocity at which the segmented free wing became unstable was between 22 and 30 ft/s . The analytical model predicts a significantly more stable system. This discrepancy between the analytical model and experimental results possibly occurs from characteristics not modeled in the analysis. An example of a characteristic that was not modeled is the small oscillation of the forward mounted counterweights along with their possible effects on the aerodynamic properties of the airfoil. During experimental testing, small oscillations of the 1 ounce counterweight were visible in both the horizontal and vertical directions. Also, the segmented free-wing mounting beam was modeled having no movement. However, in the experimental tests, the beam had a slight bending deflection that would allow the mount to have small, finite oscillations. This oscillation could have been caused by the movement of the segmented free wing or any movement in the suspension of the truck. This was not believed to affect the system as it would appear to the wings only as turbulence, however, it was not modeled so the effects are unknown. Finally, the modeling parameters used in the analytical model may have a certain amount of error possibly causing the analytical model to predict a more stable dynamic system. Examples of the parameters that may have error are the spring constant, mass moments of inertia, center of gravity position of the airfoil, and finally the aerodynamic center of the airfoil.

The uncertainty in the spring constant of the mounting beam comes from a limitation in the testing. A torque wrench was attached to the front of the supporting beam. The beam was then torqued until a particular angle of twist was achieved,

followed by recording the value from the torque wrench. A problem with this method of measuring the spring constant arises from the downward bending of the beam from the way the torque was applied. The effect of the bending of the beam on the measured torque is unknown.

The pitching and rolling mass moments of inertia were measured via a bifilar pendulum. Potential error in the pitching moment of inertia comes from the varying mass in each wing segment. The pitching mass moment of inertia for one segment was measured and assumed to apply for all of the segments of the segmented free wing. The quantity of internal wires and their position, the counterweight mass and position, and variable segment mass all contribute to an uncertainty in the pitching mass moment of inertia. For both the rolling and pitching mass moments of inertia, the damping of the displaced volume of air during the bifilar pendulum test was not modeled and ignored in all calculations of mass moments of inertia. These damping effects were ignored because there is no simple means of estimating or measuring them.

The location of the center of gravity of each individual segment varies in each segment depending on the location of the control surface wires that run laterally through the internal spaces of the airfoil aft of the spar. The segments were balanced as accurately as possible, but during flight the wires have freedom to move and can shift the center of gravity of the segment a finite amount, depending on the number of control wires running through the individual wing segment.

Variations in the surface of each wing segment can affect the location of the aerodynamic center. As determined by Xfoil, the aerodynamic center of the airfoil is shifted aft due to a small separation bubble that occurs just aft of the maximum thickness of the airfoil. However, small imperfections in the surface could cause a change in the boundary layer. Each free-wing segment was covered with a plastic

laminate. Small wrinkles and ridges were present on the surface from the laminate and could affect the boundary layer conditions of each segment. Changes in the boundary layer conditions on each segment could affect the separation bubble that occurs and therefore affect the aerodynamic center position on each free-wing segment.

5.3.5 Full Aerodynamic Model Sensitivities

The potential error in the input parameters of the system could have a large effect on the analytical model's prediction of when the system will become unstable, measured by the crossover velocity. To better understand the analytical model's sensitivities to these parameters a study was performed by slightly changing the input values and observing the change in the crossover velocity. The parameters examined were the rolling moment of inertia, pitching moment of inertia, aerodynamic center, center of gravity position, and the spring constant. Each value was varied to show the behavior in the general vicinity of the predicted value. The spring force and mass moments of inertia were varied by plus and minus 25% and 50% whereas the aerodynamic center was varied between 27% and 31% of the chord. The center of gravity position was varied from 5% aft of the spar to 3% forward of the spar.

Increasing the pitching mass moment of inertia decreases both the crossover velocity and the crossover frequency as shown in Fig. 5.14. The change in frequency is quite small when compared to the change in velocity associated with the increase in pitching mass moment of inertia. However, as you continually increase the inertia the frequency fall off rate increases. The change in crossover velocity is more extreme in the lower regions of the pitching mass moment of inertia and begins to level off as it increases to $0.008 \text{ slugs} - ft^2$.

Changes in the rolling mass moment of inertia are similar to that of the pitching mass moment of inertia. Unlike the crossover frequency associated with the pitching

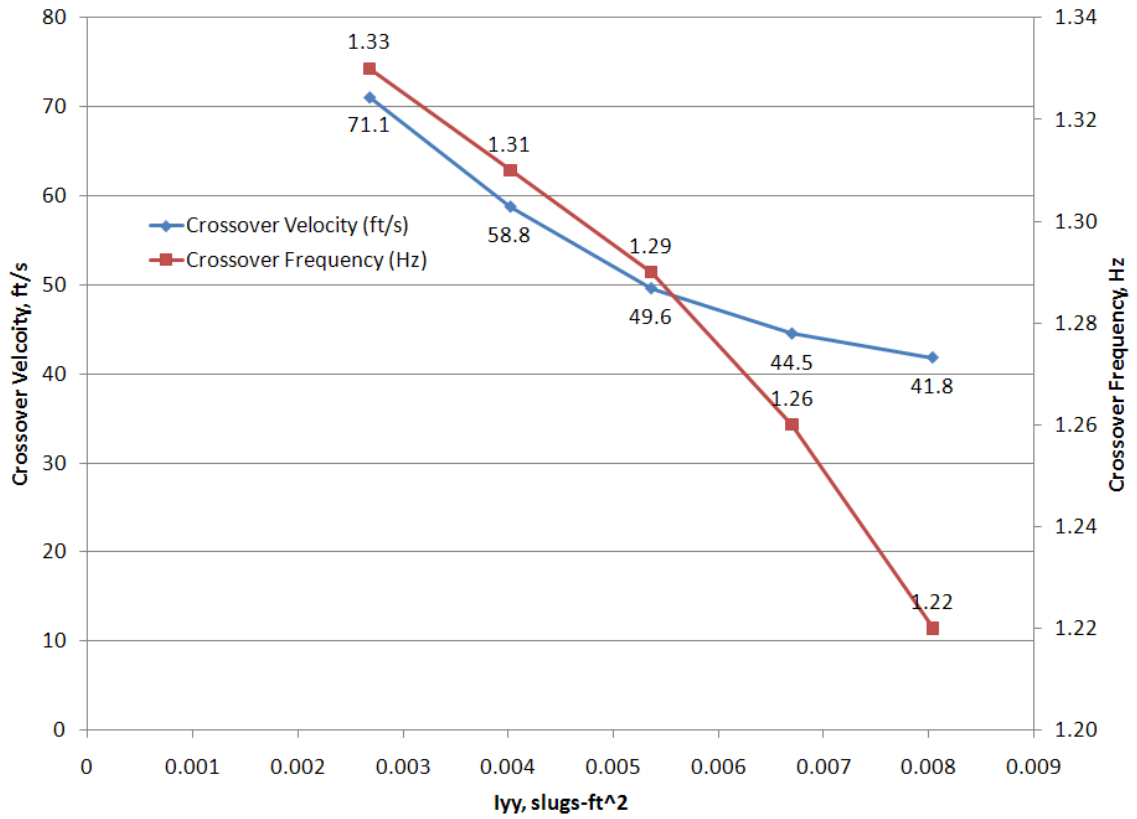


Figure 5.14: Full aerodynamic model sensitivity to changes in pitching mass moment of inertia

mass moment of inertia, the rate of change of the crossover frequency decreases as the rolling moment of inertia is increased. The crossover frequency for the changing rolling mass moment of inertia follows the same behavior as the crossover velocity. As the rolling mass moment of inertia is increased, the system becomes increasingly unstable and the crossover velocity is decreased as shown in Fig. 5.15.

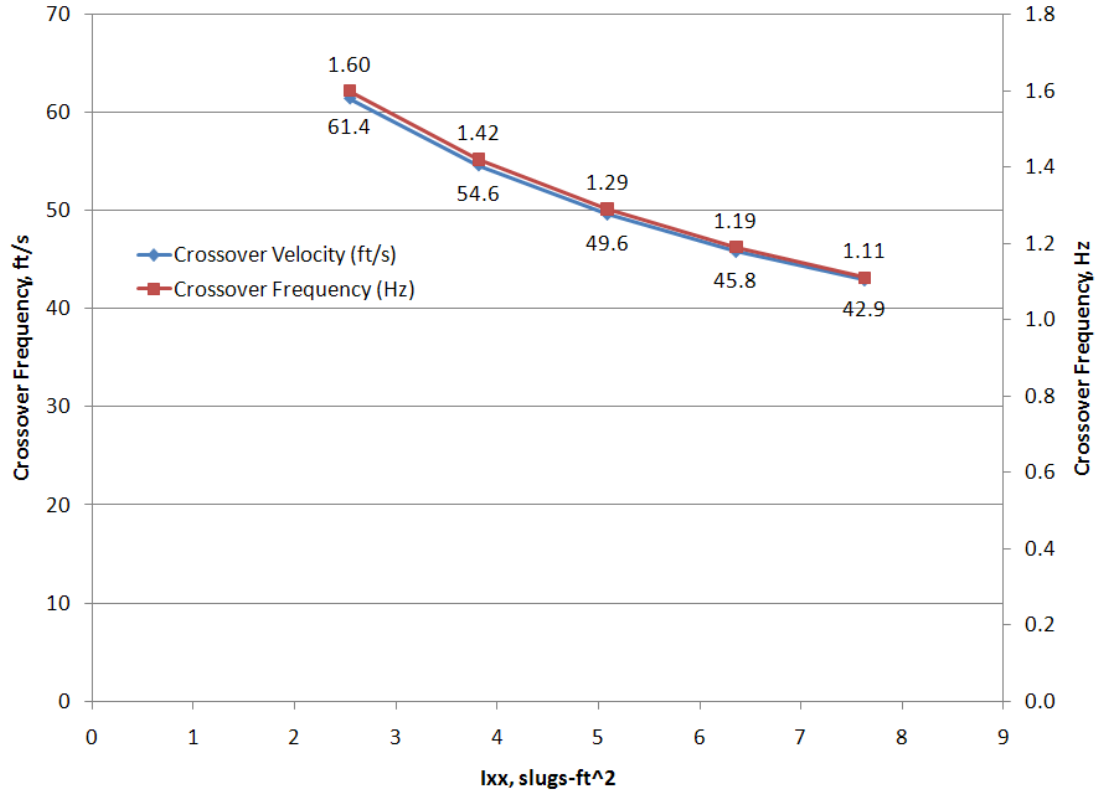


Figure 5.15: Full aerodynamic model sensitivity to changes in rolling mass moment of inertia

Shifting the aerodynamic center of the airfoil produces a similar result for the crossover velocity when compared to changes in the mass moments of inertia. The crossover frequency, however, behaves in a much different manner. As the aerodynamic center is moved aft, the crossover frequency increases almost linearly. As mentioned previously, the crossover velocity follows the same trend as the mass moments

of inertia where the changes in velocity are greater when the aerodynamic center is forward.

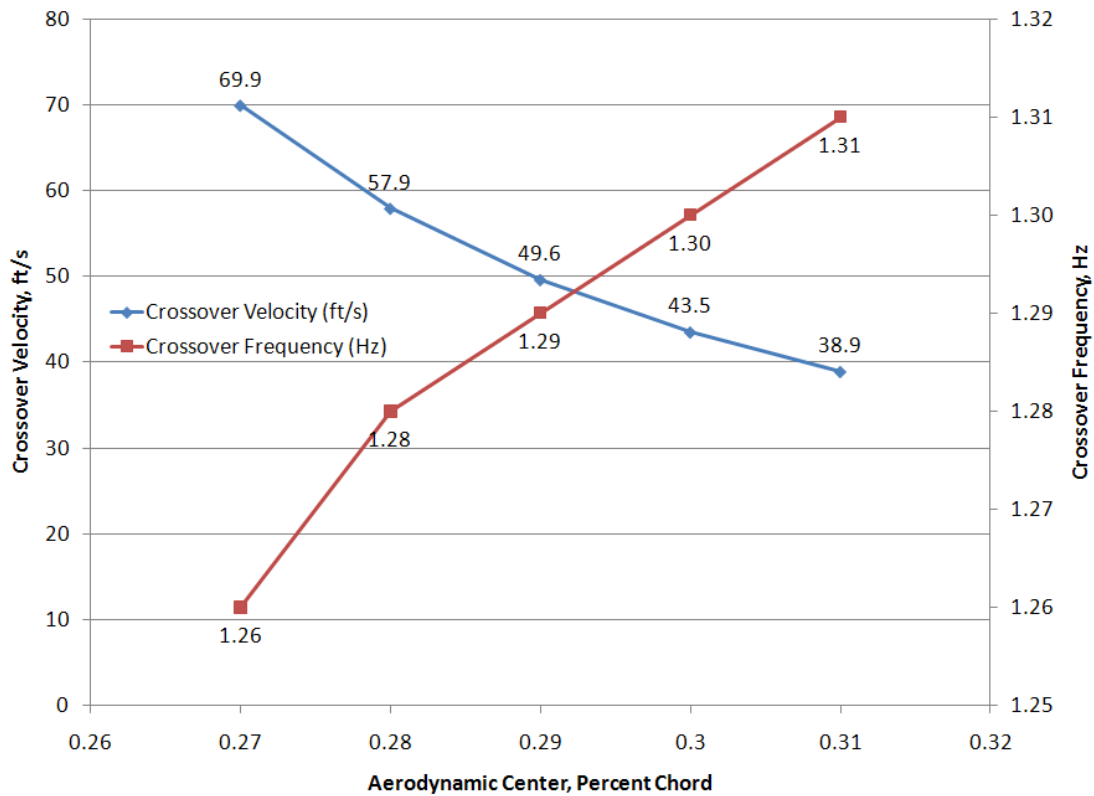


Figure 5.16: Full aerodynamic model sensitivity to changes in the aerodynamic center

Changes in the center of gravity position of each wing segment from the hinge location causes a linear change in both the crossover velocity and frequency. The crossover frequency decreases linearly as the hinge location is moved forward from behind the hinge location to ahead of the hinge location. In contrast to the crossover frequency, the crossover velocity decreases as the center of gravity position moves aft. It is believed from experience in the experimental trials that the center of gravity position is aft of the hinge location due to a shift in the position of the internal control wires during flight. The wires were housed in a chamber that allowed the wires to vary in position from 4.125 to 6.25 inches aft of the leading edge of the segment. If the

wing segments were perfectly balanced with the wires in the most forward position, the center of gravity would shift aft during flight as the wires shifted aft. This would produce a segment imbalance and a center of gravity offset of approximately 2%. If the center of gravity position was shifted 2% aft of the hinge location the predicted crossover velocity changes to 44.1 *ft/s*.

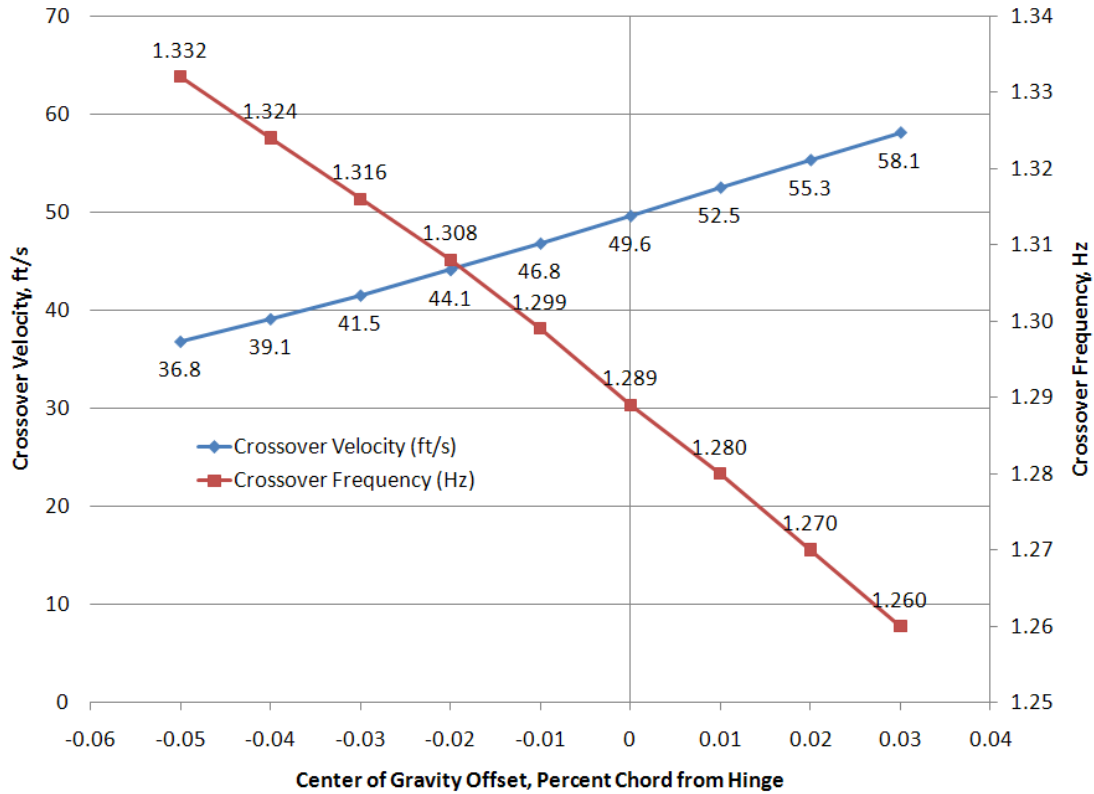


Figure 5.17: Full aerodynamic model sensitivity to changes in the center of gravity position

The spring constant was also varied to show the full aerodynamic model’s sensitivity. Figure 5.18 shows how the crossover velocity and frequency changes as the spring constant is both increased and decreased. Both the crossover velocity and frequency follow the same trend and increase as K is increased.

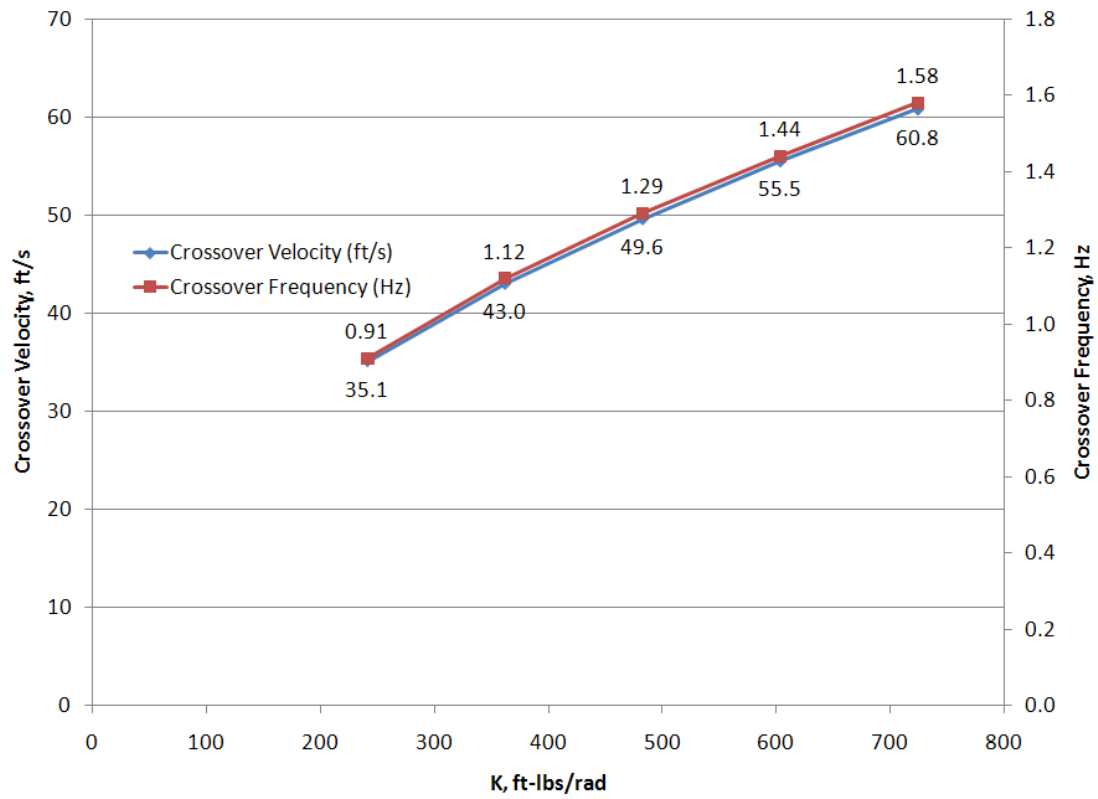


Figure 5.18: Full aerodynamic model sensitivity to changes in the spring constant K

5.3.6 Variation of Input Parameters Based Upon Error Estimates

Model parameters strongly affect the predicted crossover velocity and frequency produced by the analytical model. As discussed in Section 5.3.4, there is some uncertainty in the values that were used in the analytical model. Based upon estimations of the uncertainty, the model parameters can be modified to produce results that are in closer agreement with the experimental results. The modifications to the parameters are simply estimations of the approximate error.

The mass moments of inertia are assumed to be an overestimate due to the ignored damping of the displaced air from the spinning of the bifilar pendulum. It is estimated that the damping effect is greater in the rolling moment of inertia than the pitching moment of inertia due to the larger surface area perpendicular to the movement. The rolling mass moment of inertia has been reduced by 20% and the pitching mass moment of inertia has been decreased by 10%.

Balancing each individual wing segment was always extremely difficult due to the variability in the internal wires position. Because of the difficulty in balancing the segments, and the wires ability to move inside the segments, the center of gravity of each individual segment was most likely not centered on the hinge. The tendency of the wires to move aft in the wing segments during flight would cause the center of gravity to shift aft. The shift of the CG position aft causes an increase in the instability of the segment free-wing system. For the analytical model, the center of gravity position was shifted aft to 4% of the chord behind the hinge location.

Xfoil was used to determine the aerodynamic center of the airfoil. The value calculated by Xfoil was between 29% and 30% of the chord. However, due to surface imperfections, the boundary layer may be forced to transition earlier than it would if it were to freely transition. This causes the aerodynamic center to continue to

shift aft to approximately 30%. However, the forced transition only occurs at one location whereas imperfections that could cause a forced transitions are numerous in the plastic surface coating. Based upon the forces transition and the numerous imperfections on the surface of the airfoil, the aerodynamic center has been shifted to 31% of the chord in the analytical model to study the affect on the predicted stability.

Finally, a moderate beam deflection resulted from the applied torque during the spring constant verification and may have introduced error into the estimated spring constant, K . Because of the beam deflection, the measured torque was not as a result of a true twisting of the mounting beam and therefore is considered high. The initial analytical estimate of the spring constant, based upon published wood properties [31], was approximately $125 \text{ ft} - \text{lbs}/\text{rad}$, but since the exact species of the wood is unknown, this is just a ballpark figure. The measured value, including any deflection force of the beam, was $482.5 \text{ ft} - \text{lbs}/\text{rad}$. The large discrepancy between the two values may be an indication of the overestimation of the measured spring constant. For the analytical model, the spring constant K was reduced by 30% as an estimation of the possible error brought into the system by the beam deflection.

When the analytical model is run with these new estimates of the parameters, the results are quite promising. The root locus plot for the full aerodynamic model is similar to previous results for both the mechanically restrained and mechanically free systems. The crossover velocity and frequency for the mechanically restrained system has decreased to $29.9 \text{ ft}/\text{s}$ and the crossover frequency is 1.23 Hz. These results match the experimental results closely. In Fig. 5.20, the unstable modes are quite visible and are increasing in instability as velocity is increased. The frequency, however, is remaining almost constant as the velocity is increased.

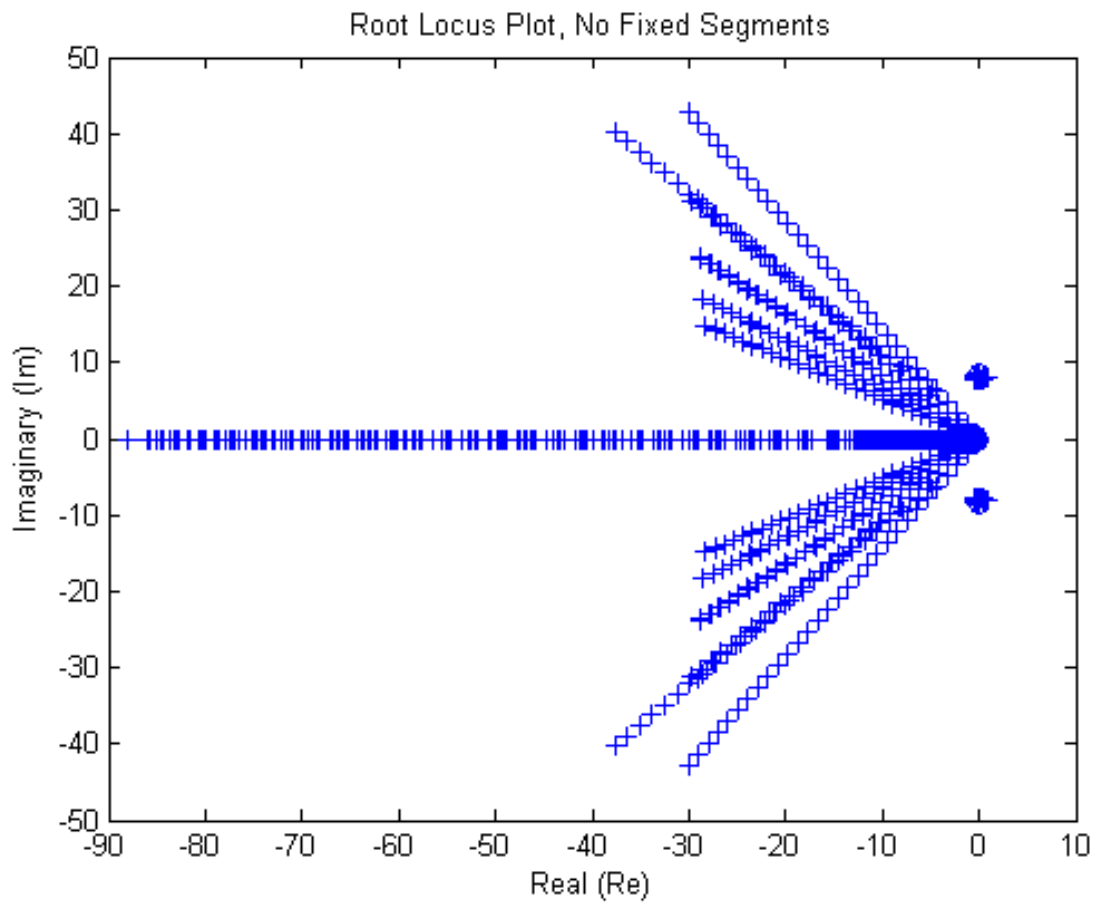


Figure 5.19: Root locus plot of the full aerodynamic model with modified input parameters but without fixed segments

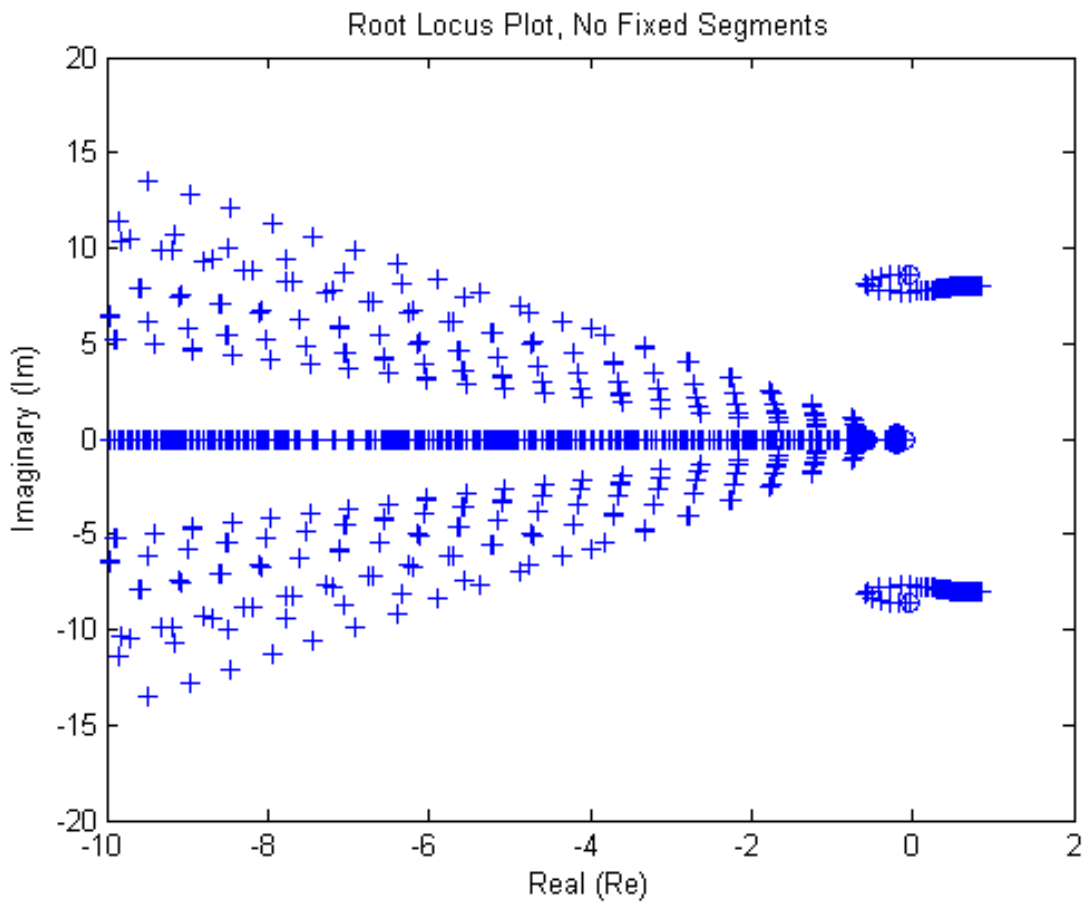


Figure 5.20: Root locus plot of the full aerodynamic model with modified input parameters but without fixed segments zoomed in to reveal unstable roots

The free-to-roll system with the modified input parameters produces the same result as the previous model. When the system is not mechanically restrained, an unstable roll mode exists immediately.

Adding the fixed segments to the modified system produces the same stabilizing results as discussed in Section 5.3.3. The unstable rolling mode in the mechanically restrained system has been stabilized by the fixed segments as it was in the analytical model without the modified inputs. Additionally, the free-to-roll system is neutrally stable just the same as the analytical model without the modified input parameters. The modified input parameters do not change the qualitative behavior of the system, they just change the velocity and frequency at which they occur. The modified input parameters in the analytical model, based on rough error estimates, produces a result very similar to the experimental results.

5.3.7 Modeling Options

The analytical model was designed so different modeling features could be turned on and off. The basic model consisted of only circulatory lift and the following features could be added: apparent mass, unsteady aerodynamics, and wake effects.

Figure 5.21 shows a root locus plot for the system using the basic aerodynamic model. In the basic model, only steady state aerodynamic calculations were included without the unsteady or apparent mass terms. Moreover, the coupling effects of the vortex wake were also neglected. The plot clearly shows the instability of the system with the cross-over from a stable to unstable system. The oscillation frequency at the velocity where the root crosses over from stable to unstable is 0.90 Hz. This is low compared to the 1.2 Hz estimated frequency from the experimental analysis. The analytical model with only the basic aerodynamic model predicts the instability will occur around 11.5 *ft/s* which is 48% lower than the experimental case.

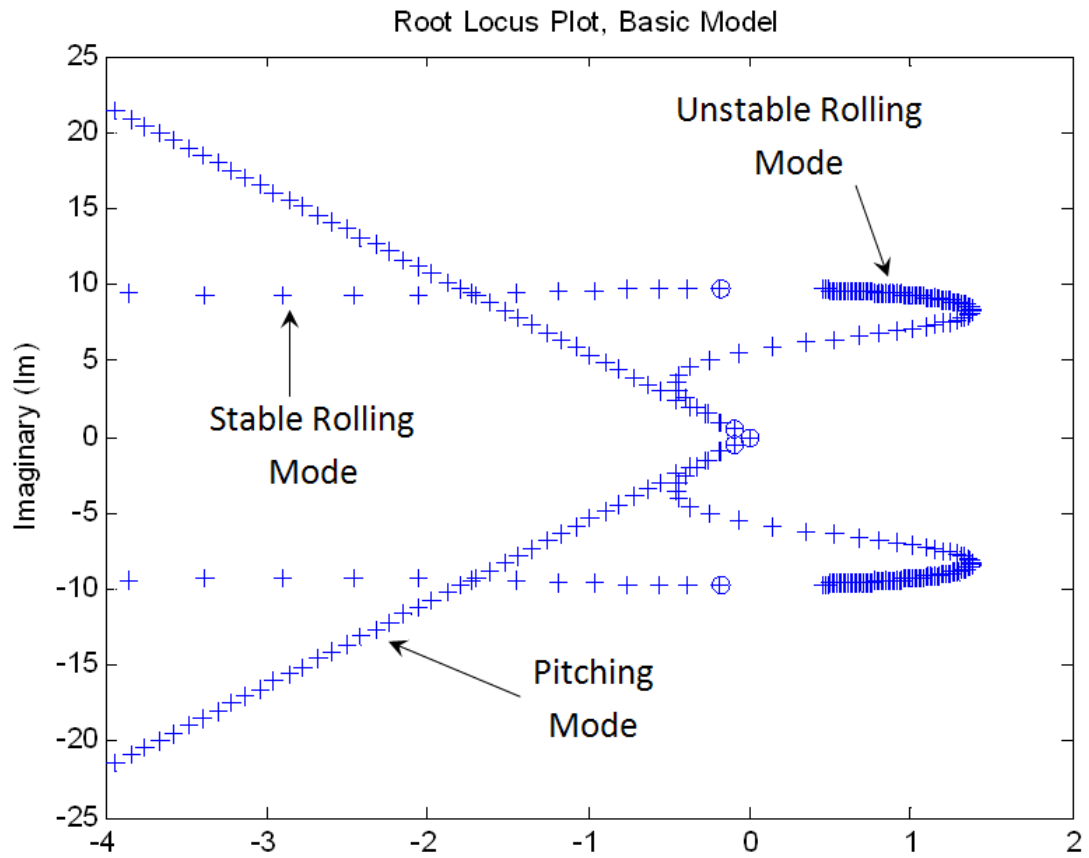


Figure 5.21: Root locus plot of the basic model

Variation of the Aerodynamic Models within the Analytical Model		
Aerodynamic Models	Crossover Velocity (ft/s)	Crossover Frequency (Hz)
Basic Model	11.5	0.90
Wake Effects	14.0	0.91
Unsteady Aerodynamics	4.8	0.32
Apparent Mass Terms	26.2	1.25
Full Model	49.6	1.29

Table 5.5: Results of the different modeling features

Figure 5.22 shows the root locus plot including the effects of the vortex wake system. With this option enabled, the analysis calculated the mutual influence of each of the wing segments on each other. The major difference between this figure and the results from the basic model is in the pitching modes. The unstable rolling mode has a different shape but the general behavior is the same. In the basic model, the pitching modes for each of the wing segments have identical eigenvalues. When wake effects are enabled however, the pitching modes of the various segments are slightly modified. As can be seen in Fig. 5.22, the pitch modes spread out as velocity is increased. The spreading of the pitching mode results from different segments having different effects on each other. Hence, their coupled oscillations are slightly different. These interactions also influence the pitch/roll instability. With the wake analysis included, the crossover velocity increased from 11.5 *ft/s* to 14.0 *ft/s*, an increase of 22%. The 14.0 *ft/s* value is closer to the experimental value of around 22 *ft/s*. The frequency of the oscillation remained almost the same at 0.91 Hz.

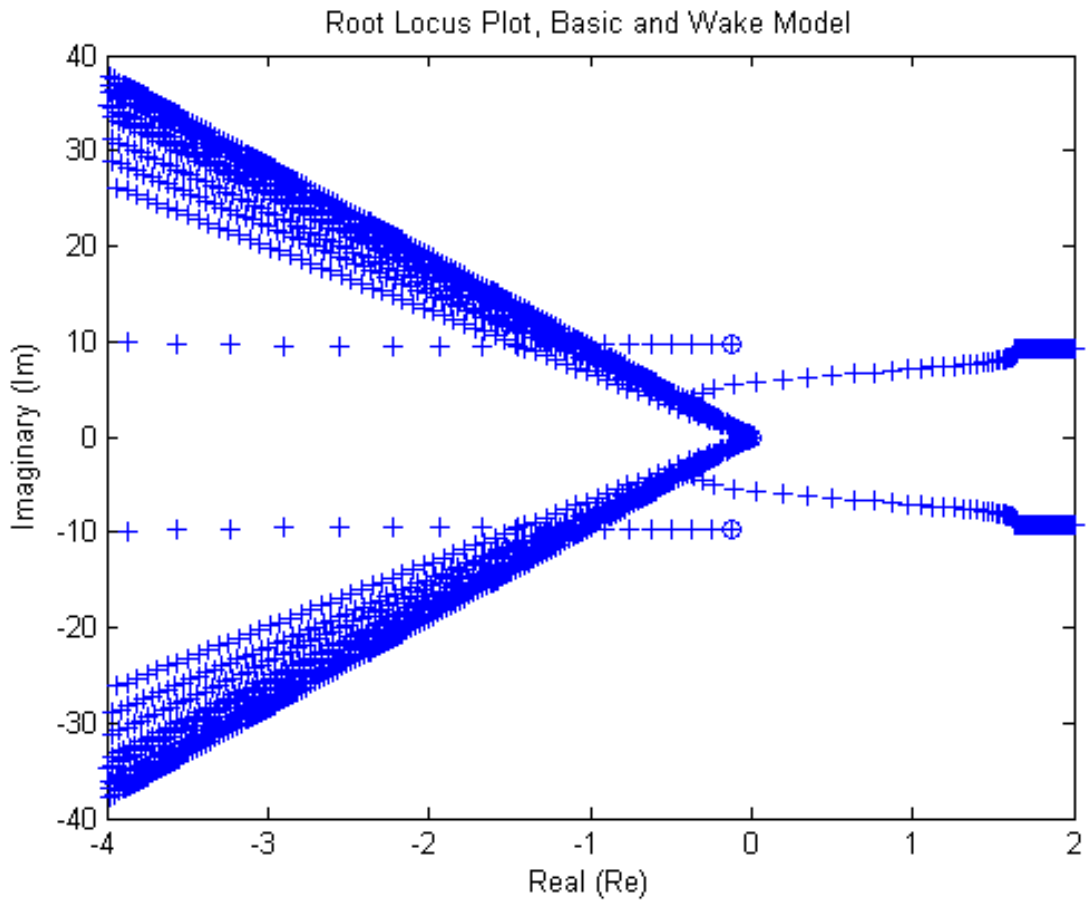


Figure 5.22: Root locus plot of the basic model with wake effects

Adding unsteady aerodynamic modeling has a larger effect as shown in Figure 5.23. In this figure, the circulatory unsteady aerodynamic terms have been included but not the apparent mass or non-circulatory terms. The same modes are present but the shape has changed. The pitching modes maintain the same frequency but the damping has decreased. The frequency of the stable roll increased compared to the basic model. The crossover velocity for the unsteady model has decreased significantly to 4.8 ft/s , a 58% drop. In addition to the changing crossover velocity, the frequency of oscillation at crossover has decreased to 0.32 Hz which is a drop of 73% from the experimental results. The addition of the unsteady model, by itself, does not closely match the experimental results.

Figure 5.24 adds the apparent mass terms to the aerodynamic model and dramatically alters the mode shapes. The apparent mass terms provide significant damping to the system which causes the crossover velocity to increase to 26.2 ft/s (a 128% increase). The frequency of the unstable rolling oscillation has also increased by 39% to 1.25 Hz. The pitching mode is much more heavily damped with the apparent mass model than the basic, wake, or unsteady models.

For the final case shown in Figure 5.25, all the modeling options were enabled. The apparent mass terms and the wake effects dominate the overall shape of the root locus plot. The effects of the wake on each segment can be seen in the pitching mode with the varying frequencies of oscillation. The unstable rolling mode has a similar appearance to the apparent mass model however the crossover velocity is much higher at 49.6 ft/s . Also, the frequency is slightly more than the apparent mass model at 1.29 Hz and is still higher than experimental results showed. Additionally, the pitching mode is highly damped as it is in the apparent mass model. The addition of the unsteady model provides additional instability to the system. With just the wake and apparent mass models the crossover velocity decreases to 44.9 ft/s even though

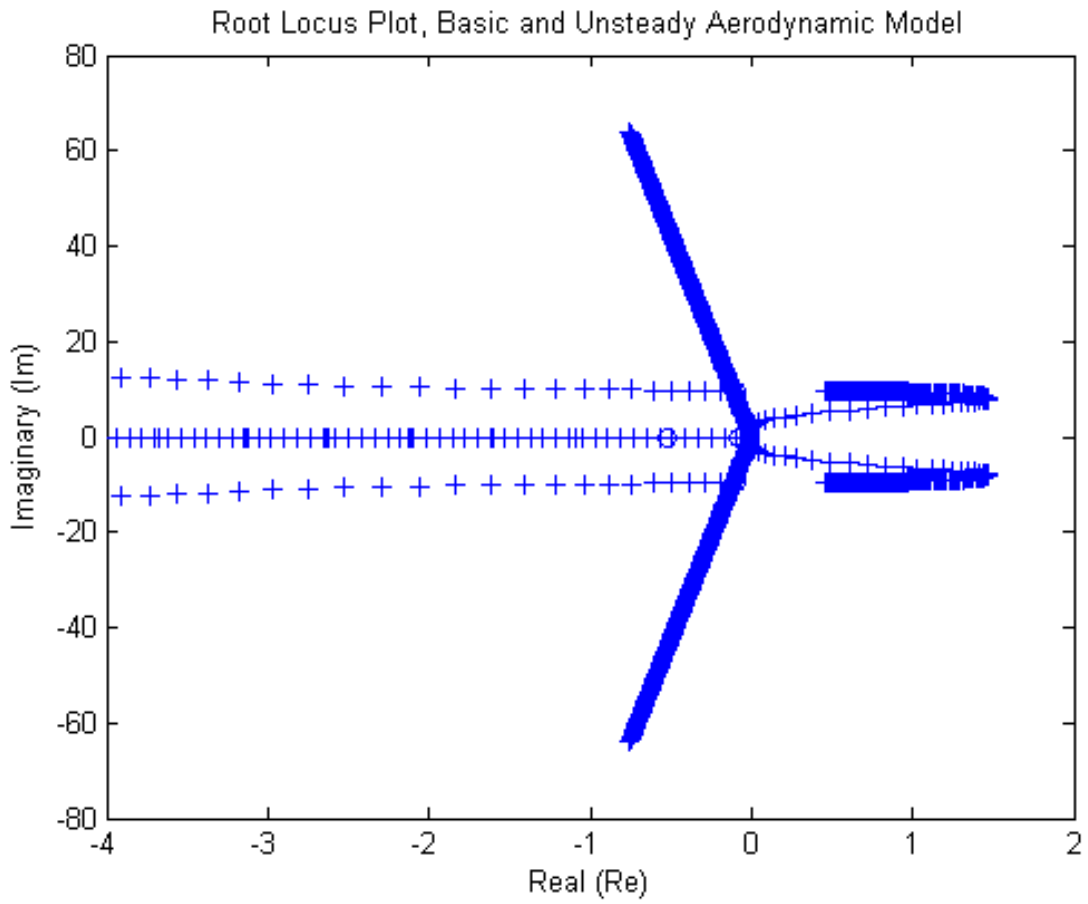


Figure 5.23: Root locus plot of the basic model with unsteady aerodynamics

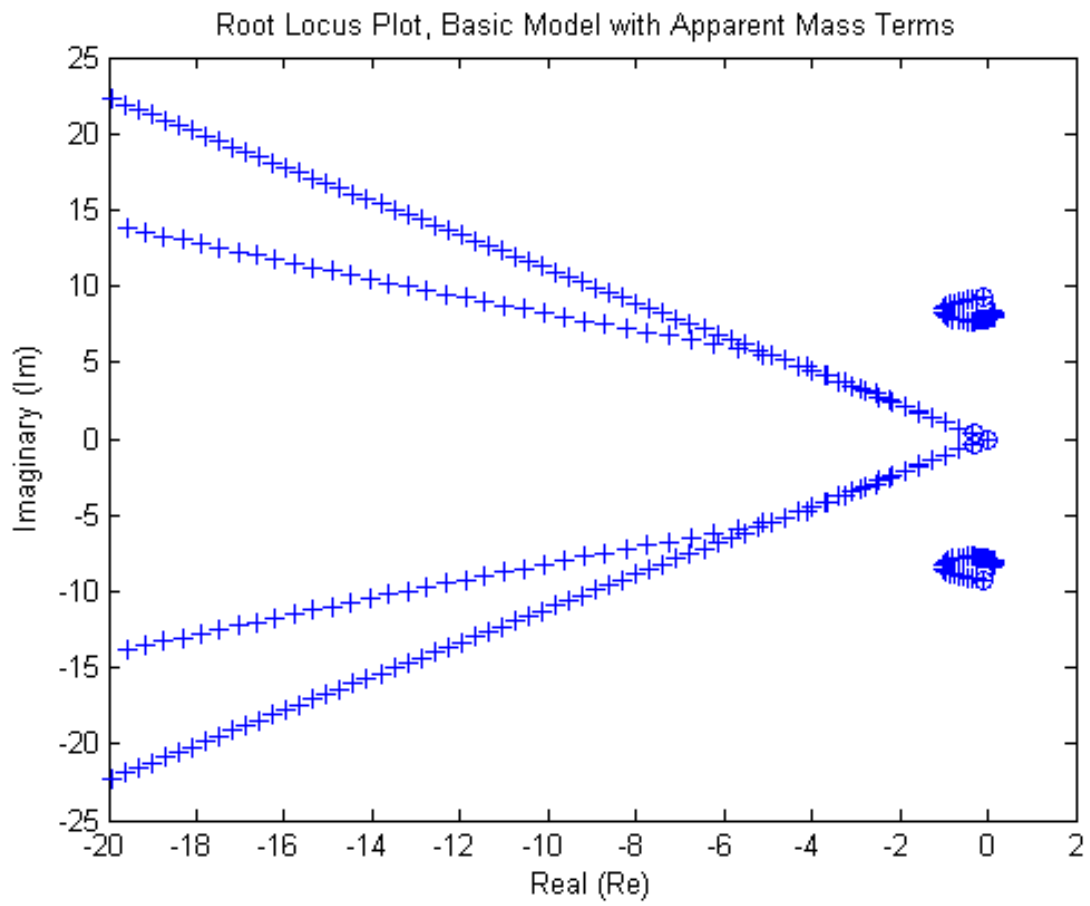


Figure 5.24: Root locus plot of the basic model with apparent mass terms

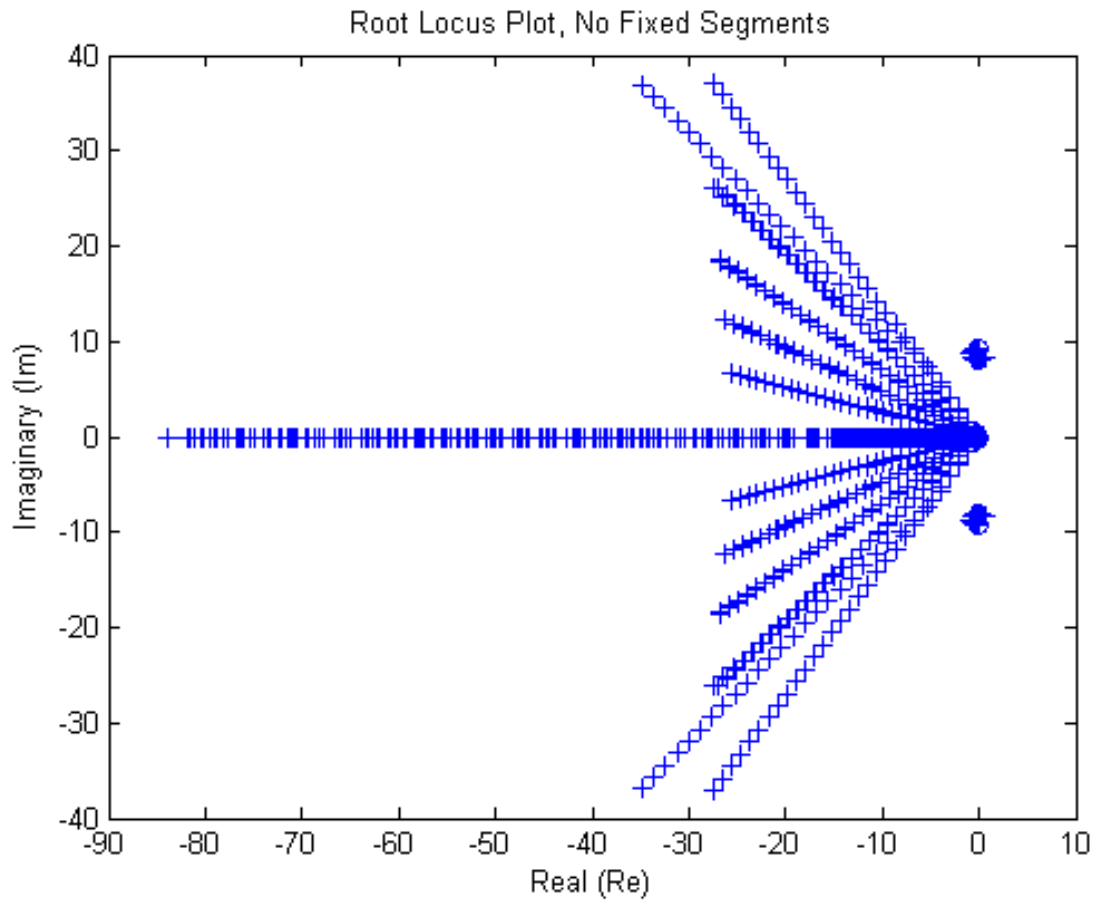


Figure 5.25: Root locus plot of the full aerodynamic model

the shape of the root locus plot is very similar to a combination of the wake models and apparent mass models. The frequency of the crossover point changes very little as you add the additional models to the wake and apparent mass models. It remains in the vicinity of 1.29 Hz. The basic model with the apparent mass terms appears to closely resemble the experimental results but due to the calculated reduced frequency unsteady aerodynamics were determined to be necessary to accurately model the aerodynamics of the system.

5.4 Wind Tunnel Model

To provide additional experimental data for validation of the analytical model, the wind tunnel model was tested again with a modified mount to allow it to rotate like the truck mount.

5.4.1 Wind Tunnel Test Results

Verification of the analytical model was performed by comparing the results from the analytical model to the wind tunnel tests. The input parameters of the analytical model had to be changed to those of the wind tunnel model. Several springs with different spring constants were obtained to test with the wind tunnel model on the modified mount. The stiffness of the spring was input into the analytical model for a prediction of the crossover velocity of the wind tunnel model. Sufficient rigidity of the spring was needed to maintain stability until at least the lower velocity bounds of the wind tunnel could be reached. The 3x4 foot closed-circuit wind tunnel reaches steady flow between 30 and 40 *ft/s*. A 0.25 inch diameter steel rod was found to be sufficient for the spring force. The distance between the hard mount in the wind tunnel and the wind tunnel model was 6 inches, connected together via the steel rod.

With a modulus of rigidity of 11,000,000 psi obtained from Raymer [32], an estimate of the spring constant K was calculated to be $58.2 \text{ ft} - \text{lbs}/\text{rad}$. With this spring constant, the estimated crossover velocity was $57.6 \text{ ft}/\text{s}$. Additionally, two other rods were made of different lengths to adjust the spring constant and crossover velocity. Using the 4 inch rod, the crossover velocity was estimated at $70.6 \text{ ft}/\text{s}$ whereas the 8 inch rod produced an estimated crossover velocity of $49.9 \text{ ft}/\text{s}$.

The velocity of the wind tunnel was increased to the estimated crossover velocity of the wind tunnel model using the six inch steel rod. At the estimated crossover velocity, the wind tunnel model remained steady and stable. As the velocity increased, the model remained stable until the mount began to oscillate vertically at approximately $70 \text{ ft}/\text{s}$. The source of the oscillation was aerodynamic flutter due to the wing aerodynamic center being well in front of the elastic axis of the mounting system. The six inch steel rod was replaced by the eight inch steel rod with the lower spring constant. The velocity was again increased slowly up to $70 \text{ ft}/\text{s}$ where the model remained steady and stable the entire time. Again, at $70 \text{ ft}/\text{s}$ the model began to oscillate vertically.

Several other springs were tested to see if the system would become unstable. Spring constants with values of $5.3 \text{ ft} - \text{lbs}/\text{rad}$ and $26.5 \text{ ft} - \text{lbs}/\text{rad}$ were tested. Both springs, when placed on the model and tested, didn't allow the system to become unstable. The wind tunnel model remained stable at velocities exceeding $70 \text{ ft}/\text{s}$. Because of the continued stability of the wind tunnel model, the spring constant was drastically reduced to $0.0357 \text{ ft} - \text{lbs}/\text{rad}$. The wind tunnel velocity was continually increased to $120 \text{ ft}/\text{s}$ without any effect on the stability of the model. The wind tunnel model continued to remain steady and stable at the high velocity.

5.4.2 System Properties

The number of wing segments was reduced to six and the mass moments of inertia was adjusted for the physical properties of the wind tunnel model. The bifilar pendulum described in Section 5.3.1 was used to measure the mass moments of inertia. The pitching mass moment was changed to $0.0002 \text{ slugs} - ft^2$ and the rolling mass moment of inertia was changed to $0.153 \text{ slugs} - ft^2$.

5.4.3 Analysis of Results

Additional tests of the wind tunnel model were performed as a verification of the analytical model results. The analytical model was modified to predict the stability of the wind tunnel model with different spring constants. The initially estimated crossover velocity using the steel rod described in Section 5.4.1 was approximately 57.6 ft/s with a frequency of 3.0 Hz . The root locus plot for the wind tunnel model is shown in Fig. 5.26.

Several different explanations were considered for the discrepancy between the predicted behavior and observed behavior of the wind tunnel model. One hypothesis was that friction in the roll and pitch bearings was affecting the results. To evaluate this hypothesis, friction terms were added to the equations of motion as described in Section 4.5. The friction terms provide increased damping to the system, but the exact values were unknown. In order to find approximate values of the friction coefficients that would reproduce the observed behavior, the values were varied in order to have the computer model predict stability up to 120 ft/s . The rolling friction was the larger driver and therefore was varied to determine the value of pitching friction required to maintain the stability at 120 ft/s . A plot of the combination of friction coefficients that provided stability at 120 ft/s is shown in Fig. 5.27. The combination

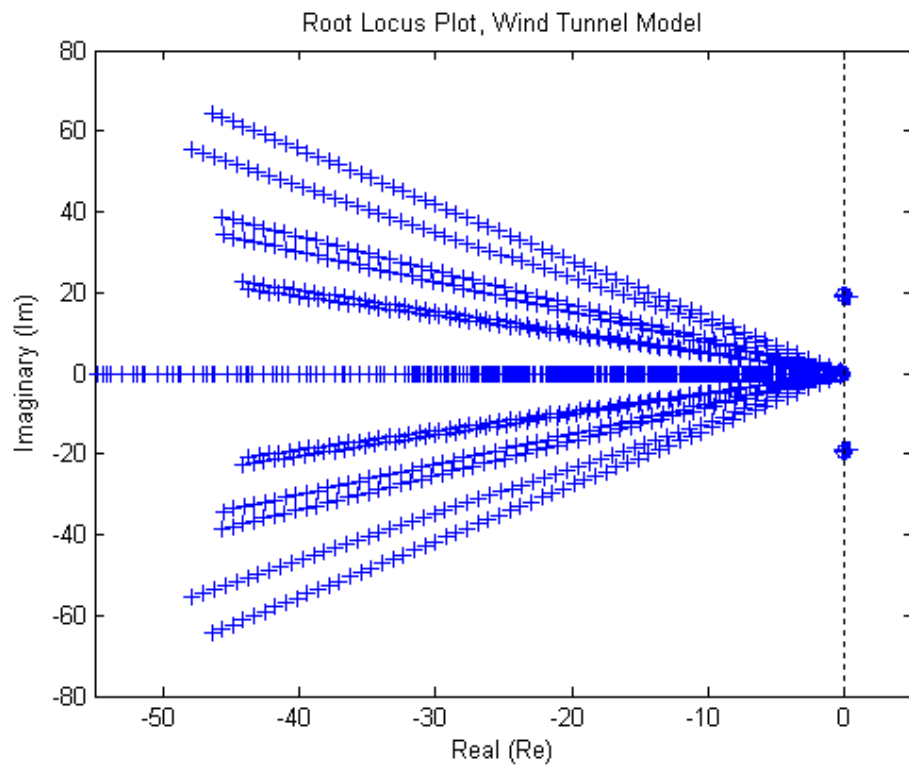


Figure 5.26: Root locus plot for the wind tunnel model

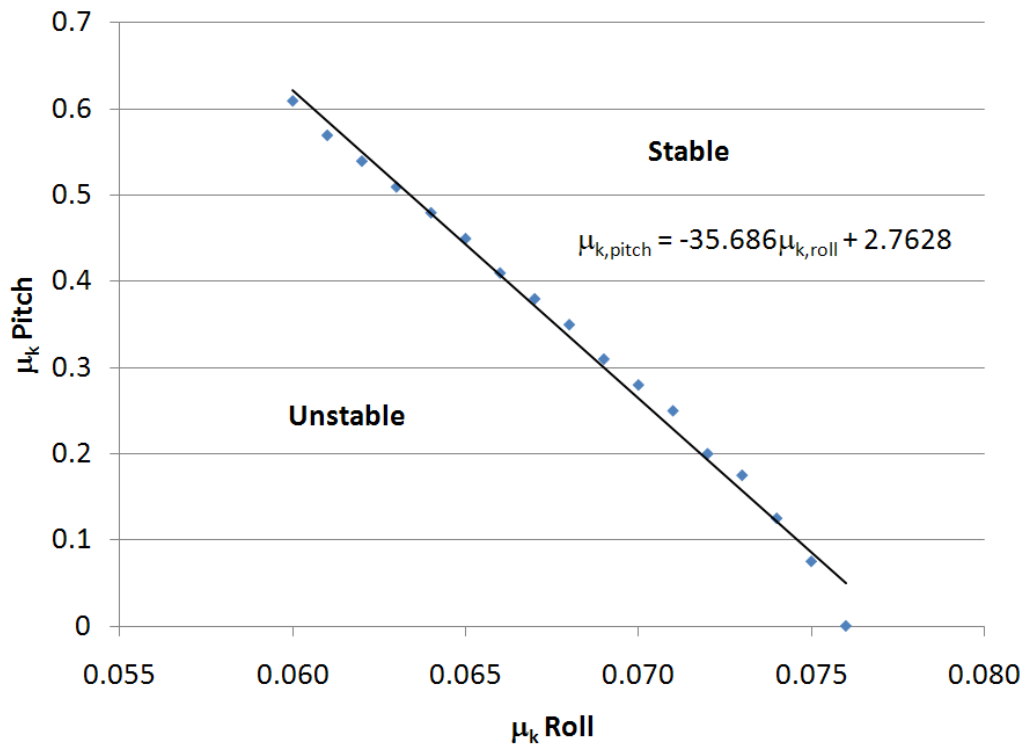


Figure 5.27: Friction coefficients for maintained stability with unsteady aerodynamics

of the coefficient of friction for roll and pitch has to be greater than the linear trend of $35.686\mu_{k,roll} + \mu_{k,pitch} = 2.7628$. For all combinations of the friction coefficients greater than or equal to 2.7628, the model is stable at or above 120 *ft/s*. Since the wind tunnel model remained stable to 120 *ft/s*, it is inferred that the combination of the coefficients of friction is at or above the trend line.

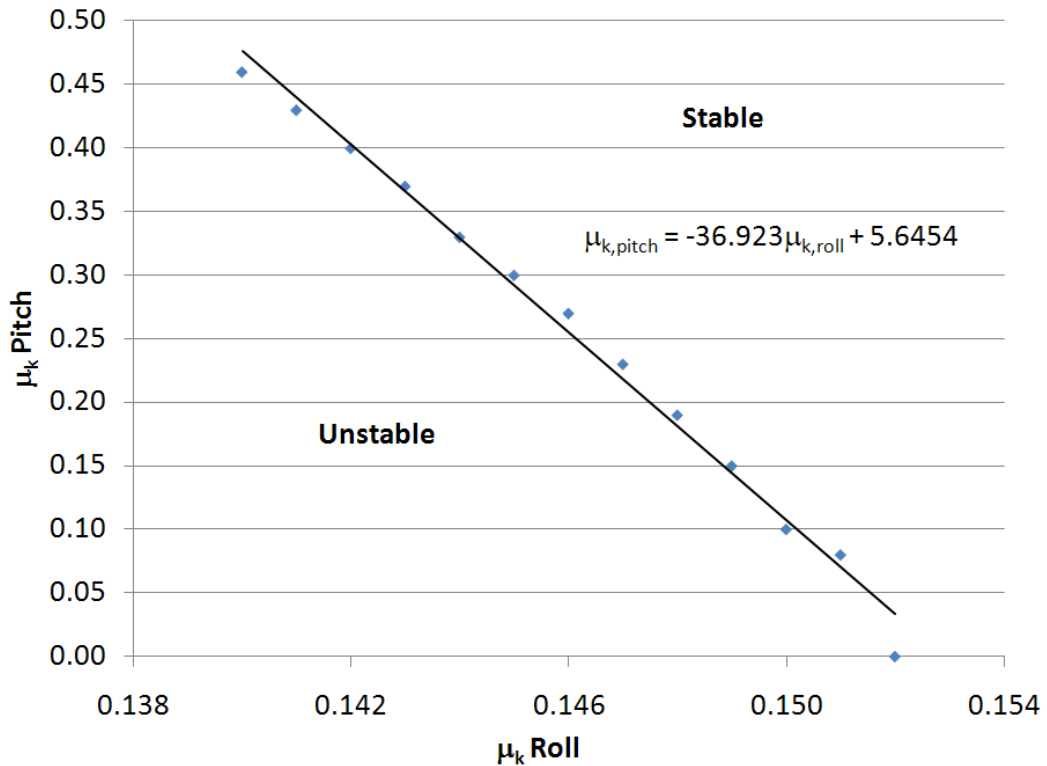


Figure 5.28: Friction coefficients for maintained stability without unsteady aerodynamics

In contrast to the larger experimental model, for the wind tunnel model unsteady aerodynamics were determined to be unnecessary because the reduced frequency ranged from $2.63e-3$ to $1.34e-3$, depending on the value of the rolling friction coefficient. When unsteady aerodynamics were removed from the system, the same linear trend in the friction coefficients occur but the values were slightly changed as shown in Fig. 5.28. The new linear trend line is $36.923\mu_{k,roll} + \mu_{k,pitch} = 5.6454$. The

required value of the rolling friction for stability at 120 *ft/s* has been increased slightly but the relationship of the pitching friction compared to the rolling friction remains approximately the same. Just as with the unsteady aerodynamics on, all combinations of pitching and rolling friction coefficients that are greater than or equal to the linear trend provide stability to the model at speeds greater than or equal to 120 *ft/s*.

5.4.4 Friction Discussion

The moment produced by the friction could be determined by estimating the angular velocity of the rolling and pitching motions. The pitching and rolling frictions were modeled as $M = \mu_{k_{pitch}}\dot{\theta}$ and $M = \mu_{k_{roll}}\dot{\phi}$ respectively with the values of $\mu_{k_{pitch}}$ and $\mu_{k_{roll}}$ being input parameters in the analytical model as described above. If the friction coefficient between the steel rod and aluminum block of the wind tunnel model exceeds the largest rolling coefficient value in Figs. 5.27 and 5.28, then the model would always be stable up to 120 *ft/s*.

The angular velocity was modeled by

$$\dot{\phi}(t) = A\omega \cos \omega t \quad (5.7)$$

The maximum angular velocity occurs when $\cos \omega t = 1$ so the angular velocity simplifies to

$$\dot{\phi}(t) = A\omega \quad (5.8)$$

The frequency, ω , and the rolling friction coefficient, $\mu_{k_{roll}}$, come from the analytical model and were 0.473 and 0.076 respectively. A maximum roll angle of 10 degrees was estimated and the total moment induced by the rolling friction was calculated to be

0.00629 *ft – lbs*. A dry bearing was used and the friction torque could be calculated as

$$M = P\mu\frac{d}{2} \tag{5.9}$$

where P is the net loading force, d is the shaft diameter, and μ is the dimensionless friction coefficient between the two bearing materials.

The net loading force was the difference between the system weight and the lift produced by the wind tunnel model. The total system weight for the wind tunnel model was 5.164 *lbs*. An estimate of the total lift produced by the wind tunnel model at 120 *ft/s* was used to determine the net load on the bearing to be used in Eqn. 5.9. A C_L of 0.2 was used for the lift estimate based upon the 5 degree control surface deflection. The estimated lift produced by the wind tunnel model at 120 *ft/s* was 7.43 *lbs* which gives a net force on the bearing surface of 2.266 *lbs*. Setting Eqns. 5.8 and 5.9 equal to each other, a value for μ was calculated to be 0.27. From Table 5.6,

Materials in Contact	Static Coefficient of Friction μ_s	Kinetic Coefficient of Friction μ_k
Aluminum on steel	0.60	0.50
Brass on steel	0.50	0.45
Copper on cast iron	1.00	0.30
Copper on glass	0.70	0.50
Copper on steel	0.55	0.35
Glass on glass	0.90	0.40
Hemp rope on wood	0.50	0.40
Leather on wood	0.55	0.45
Oak on oak (parallel to grain)	0.65	0.50
Rubber tire on dry concrete	0.90	0.70
Rubber tire on wet concrete	0.70	0.50
Steel on steel	0.45	0.35
Steel on ice	0.10	0.05
Teflon on Teflon	0.04	0.04
Teflon on steel	0.05	0.05
Wood on wood (dry)	0.35	0.15

Table 5.6: Selected values of coefficients of friction [33]

the coefficient of friction between steel and aluminum is 0.5 which is almost double the required coefficient of friction to provide stability to the wind tunnel model up to a velocity of 120 *ft/s*.

When unsteady aerodynamics were turned off, the rolling coefficient estimated by the analytical model changed to 0.152 with a slight reduction of the frequency to 0.472 *rad/s*. Using the same process as described above, an estimated dimensionless coefficient of friction was calculated as 0.5 which is the same as the coefficient of friction between aluminum and steel [33]. From the estimates of the angular velocity and the lift produced by the model, the coefficient of friction between aluminum and steel is sufficient to provide stability to the wind tunnel model up to speeds of 120 *ft/s*.

The 6 inch steel rod provided a spring constant of 58.2 *ft-lbs/rad* from which the analytical model predicted a crossover velocity of 57.6 *ft/s*. The wind tunnel model remained stable up to 70 *ft/s* before the system began to oscillate up and down and the test terminated. The system did not have a rolling bearing and therefore the only friction present in the system was from the pitch bearing of each wing segment. The two bearing surfaces consisted of a steel spar and a brass tube inside each segment which rotated about the spar. For this system, the pitching angular velocity was estimated using the same method as the rolling angular velocity. The amplitude was 5 degrees with a frequency of 19.046 *rad/s*. The estimated lift produced by a single segment was 0.388 *lbs*. A $\mu_{k_{pitch}}$ of 0.0011 provided a crossover velocity of greater than 70 *ft/s* in the analytical model. Solving for the dimensionless coefficient of friction, the value of friction required to stabilize the system was 0.45 which is equal to the coefficient of friction between brass and steel provided by Muvdi in Table 5.6 [33].

Friction forces provide damping to the wind tunnel model and were significant enough to provide stability to the system throughout all tested velocities. The coefficients required to maintain stability of the system for both the large spring constant and the small spring constant were within experimental values provided by Muvdi.

CHAPTER 6

CONCLUSIONS

A wind tunnel model of the segmented free wing was constructed and tested in the Auburn University wind tunnel. Initial results from the wind tunnel tests showed a 64% reduction in the rolling moment coefficient when compared to a conventional free wing and a 29% reduction compared to a torsionally free left and right free wing. These positive results showed that the segmented free wing does have the capability to respond to both time-varying and span-varying turbulence.

After the initial testing of the wind tunnel model, a conceptual model of a segmented free wing was designed and fabricated at Auburn University. Initial testing was conducted by mounting the segmented free wing on a truck for aerodynamic testing. A repeatable divergent rolling oscillation emerged at velocities between 22 and 29 *ft/s* when the segmented free wing was mechanically restrained in roll. When allowed to roll freely, the segmented free wing would roll over to the left or right but would not oscillate back. Once the wing rolled over, the wing remained resting against the stop. From previous results published by Porter and Brown [3], the divergent mode was presumed to be the divergent spiral mode associated with free wing when the left and right wings are allowed to be torsionally independent for each other.

Several modifications to the segmented free-wing properties were made in an attempt to stabilize the system and included changing the rolling mass moment of inertia, the center of gravity position, and the number of segments. None of the modifications to the properties increased the stability of the segmented free wing. The crossover velocity at which the wings began to oscillate in the mechanically

restrained system was virtually unchanged and a large change in the frequency of the oscillation was not seen.

The segmented free-wing design was modified by adding fixed segments to the wing tips varying in size from six inches to 24 inches in span. All the fixed segments provided dynamic stability to the system for all experimental velocities. When the system was allowed to freely roll, the fixed segments provided greater stability, but overall, the system was only neutrally stable. With the 24 inch segments, the system was capable of being trimmed, but no damping occurred if the system was perturbed. However, the divergent mode that was seen previously did not occur. The segmented free wing with the six-inch fixed segments was capable of being trimmed but was extremely sensitive to any kind of perturbation.

An analytical model was developed as a result of the experimental testing of the segmented free wing. The computer model, using eigen analysis, was successfully able to predict the divergent oscillation in the mechanically restrained system and the divergent mode in the mechanically free system. The velocity at which the analytical model predicted the oscillation to occur was higher than what occurred in experimentation. Errors in the model parameters used in the model may have contributed to this discrepancy. When the parameters were modified based upon estimates of the error, the same divergent modes were predicted but the crossover velocity at which the oscillation occurred dropped to 29.9 ft/s , which is within the upper bound of the experimental velocity. When the fixed segments were attached in the analytical model, the results matched the experimental results; the oscillation was damped out and the system was dynamically stable in the mechanically restrained system and neutrally stable in the free-to-roll system.

Finally, a wind tunnel model was tested to verify the analytical model with mixed results. The wind tunnel provided positive preliminary results of the responsiveness of

the segmented free-wing design to adverse conditions by having the largest reduction in the rolling moment when compared to the other configurations. However, the wind tunnel model failed to oscillate at the predicted velocity, but due to the smaller aerodynamic forces, friction was believed to be a larger driver in that system. A lower bound for the combination of the rolling and pitching friction coefficients was developed. Friction coefficients above those bounds provide a stable wind tunnel model up through all tested velocities. Estimates of the friction coefficients required to stabilize the wind tunnel model were calculated. The calculated friction coefficients were within experimental values and thus friction in the system was sufficient to stabilize the wind tunnel model at all tested velocities.

Overall, the segmented free-wing conceptual design is intended for use in adverse environments where span varying conditions are a significant problem. This design is most useful in the High Altitude, Long Endurance (HALE) aircraft design area where the transition through the troposphere can be extremely hazardous and potentially fatal to the vehicle. Initial results show promise in the capability in dealing with the span varying turbulence, but this research focused mainly on the dynamic stability of the segmented free-wing conceptual design.

CHAPTER 7

FUTURE WORK

Additional studies need to be performed to truly understand the abilities of the segmented free wing to adjust to spanwise varying turbulence. Initial results were positive but additional tests must be conducted. Aerodynamic properties and control characteristics such as roll rate need to be determined in order to experimentally fly the segmented free wing. Additionally, the ratio of the area of the fixed segments compared to the wing area of the free-wing segments for sufficient dynamic stability needs to be determined. Finally, the ability to control the segmented free wing needs to be determined due to the lack of damping from perturbations due to the neutrally stable free-to-roll system.

BIBLIOGRAPHY

- [1] Noll, T. E., “Investigation of the Helios Prototype Aircraft Mishap,” NASA Langley Research Center, Jan. 2004, http://www.nasa.gov/pdf/64317main_helios.pdf [retrieved 22 February 2009].
- [2] Crouse Jr., G. L., “Design for Passenger Comfort and All Weather Operation,” *AIAA Aviation Technology, Integration, and Operations Conference*, Belfast, Northern Ireland, Sept. 2007.
- [3] Porter, R. F. and Brown Jr., J. H., “Evaluation of the Gust-Alleviation Characteristics and Handling Qualities of a Free-wing Aircraft,” NASA CR-1523, Apr. 1970.
- [4] Shearer, C. M. and Cesnik, C. E. S., “Nonlinear Flight Dynamics of Very Flexible Aircraft,” *AIAA Journal of Aircraft*, Vol. 44, No. 5, 2007, pp. 1528–1545.
- [5] Cesnik, C. E. S. and Brown, E. L., “Active Wing Warping Control of a Joined-Wing Airplane Configuration,” *Proceedings of the 44th AIAA/ASME/ASCE/AHS Structures, Structural Dynamics, and Materials Conference*, Norfolk, VA, 2003.
- [6] Karpel, “Design for Active Flutter Suppression and Gust Alleviation Using State-Space Aeroelastic Modeling,” *AIAA Journal of Aircraft*, Vol. 19, No. 3, 1982, pp. 221–227.
- [7] Rennie, R. M. and Jumper, E. J., “Gust Alleviation Using Trailing-Edge Flaps,” *37th AIAA Aerospace Sciences Meeting and Exhibit*, Reno, NV, Jan. 1999.
- [8] Jones, R. T., “The Unsteady Lift of a Wing of Finite Aspect Ratio,” NACA Rept. 681, 1941.
- [9] Moulin, B. and Karpel, M., “Gust Loads Alleviation Using Special Control Surfaces,” *AIAA Journal of Aircraft*, Vol. 44, No. 1, 2007, pp. 17–25.
- [10] Block, J. and Gilliat, H., “Active Control of an Aeroelastic Structure,” *35th AIAA Aerospace Sciences Meeting & Exhibit*, Reno, NV, Jan. 1997.

- [11] Cox, C., Gopalarathnam, A., and Hall Jr., C. E., “Development of Stable Automated Cruise Flap for an Aircraft with Adaptive Wing,” *AIAA Journal of Aircraft*, Vol. 46, No. 1, 2009, pp. 301–311.
- [12] Pettit, C. L. and Grandhi, R., “Optimization of a Wing Structure for Gust Response and Aileron Effectiveness,” *AIAA Journal of Aircraft*, Vol. 40, No. 6, 2003, pp. 1185–1191.
- [13] Nam, C. and Chattopadhyay, A., “Optimal Wing Planform Design for Aeroelastic Control,” *AIAA Journal*, Vol. 38, No. 8, 2000, pp. 1465–1470.
- [14] Chattopadhyay, A., Seeley, C. E., and Jha, R., “Aeroelastic tailoring Using Piezoelectric Actuation and Hybrid Optimization,” *Smart Materials and Structures*, Vol. 8, No. 1, 1999, pp. 83–91.
- [15] Lazarus, K. B., Crawley, E. F., and Lin, C. Y., “Multivariable Active Lifting Surface Control Using Strain Actuation: Analytical and Experimental Results,” *AIAA Journal of Aircraft*, Vol. 34, No. 3, 1997, pp. 313–321.
- [16] Ormiston, R. A., “Experimental Investigation of Stability and Stall Flutter of a Free-Floating Wing V/STOL Model,” NASA TN D-6831, June 1972.
- [17] Porter, R. F., Luce, R. G., and Brown Jr., J. H., “Investigation of the Applicability of the Free-Wing Principle to Light, General Aviation Aircraft,” NASA CR-2046, June 1972.
- [18] Porter, R. F., Hall, D. W., Brown Jr., J. H., and Gregorek, G. M., “Analytical Study of a Free-Wing/Free-Trimmed Concept,” NASA-2378, Feb. 1978.
- [19] Kraeger, A. M., “Free-Wing Unmanned Aerial Vehicle as a Microgravity Facility,” *AIAA Journal of Guidance, Control, and Dynamics*, Vol. 29, No. 3, 2006, pp. 579–587.
- [20] Drela, M. and Giles, M. B., “Viscous-Inviscid Analysis of Transonic and Low Reynolds Number Airfoils,” *AIAA Journal*, Vol. 25, No. 10, Oct. 1987, pp. 1347–1355.
- [21] Drela, M., “XFOIL: An Analysis and Design System for Low Reynolds Number Airfoils,” *Low Reynolds Number Aerodynamics*, edited by T. J. Mueller (editor), Lecture Notes in Engineering #54, Springer Verlag, New York, 1989.
- [22] Fung, Y. C., *An Introduction to the Theory of Aeroelasticity*, Galcit Aeronautical Series, John Wiley & Sons, Inc., New York, 1955.
- [23] Bisplinghoff, R. L. and Ashley, H., *Principles of Aeroelasticity*, 1st ed., Dover Publications, Inc., New York, 1962.

- [24] Johnson, W., *Helicopter Theory*, Dover Publications, Inc., New York, 1994.
- [25] Rainey, A. G., “Measurement of Aerodynamic Forces for Various Mean Angles of Attack on an Airfoil Oscillating in Pitch and on Two Finite-Span Wings Oscillating in Bending with Emphasis on Damping in the Stall,” NACA-TR-1305, 1957.
- [26] Bertin Jr., J. J. and Smith, M. L., *Aerodynamics for Engineers*, 1st ed., Prentice-Hall, Inc., New Jersey, 1979.
- [27] Anderson Jr., J. D., *Fundamentals of Aerodynamics*, 4th ed., McGraw-Hill, International Version, New York, 2007.
- [28] Ginsberg, J., *Engineering Dynamics*, 1st ed., Cambridge University Press, New York, 2008.
- [29] Then, J. W. and Chiang, K. B., “Experimental Determination of Moments of Inertia by the Bifilar Pendulum Method,” *American Journal of Physics*, Vol. 38, No. 4, April 1970, pp. 537–539.
- [30] Hibbeler, R. C., *Statics and Mechanics of Materials*, 2nd ed., Pearson Prentice Hall, Upper Saddle River, New Jersey, 2008.
- [31] Forest Products Laboratory, *Wood Handbook-Wood as an Engineering Material*, US Department of Agriculture, Madison, WI, 1999.
- [32] Raymer, D. P., *Aircraft Design: A Conceptual Approach*, 4th ed., Education Series, American Institute of Aeronautics and Astronautics, Inc., Reston, VA, 2006.
- [33] Muvdi, B. B., Al-Khafaji, A. W., and McNabb, J. W., *Statics for Engineers*, Springer-Verlag, New York, 1997.